Elsevier Editorial System(tm) for Lithos
Manuscript Draft

Manuscript Number: LITHOS8730R3

Title: Early Devonian mafic igneous rocks in the East Kunlun Orogen, NW China: Implications for the transition from the Proto- to Paleo-Tethys oceans

Article Type: Regular Article

Keywords: Mafic igneous rocks; Post-collisional; Early continental rifting; Proto- and Paleo-Tethys oceans; East Kunlun

Corresponding Author: Dr. Jinlong Dong, Ph.D.

Corresponding Author's Institution: Peking University

First Author: Jinlong Dong, Ph.D.

Order of Authors: Jinlong Dong, Ph.D.; Shuguang Song, Ph.D.; Li Su, Ph.D.; Mark B. Allen, Ph.D.; Yanguang Li, Master; Chao Wang, Ph.D.

Abstract: The tectonic evolution of the Proto- and Paleo-Tethys oceans had a significant influence on ocean-continent distributions in East Asia in the Phanerozoic, and major implications for continental growth in the region. However, it remains ambiguous when and how the Proto-Tethys Ocean transformed into the Paleo-Tethys Ocean. Here we present petrologic, mineralogical, chronological and geochemical data for Early Devonian mafic igneous rocks, located in the East Kunlun Orogen. The mafic igneous rocks include basaltic lavas and diabase dykes, and are tholeiitic in composition. Geochemical and Sr-Nd isotopic data indicate that the basaltic lavas were derived from melting of a spinel-bearing asthenospheric mantle (E-MORB) at normal mantle potential temperatures (1384-1400 °C) with negligible (1-4%) crustal contamination. The diabase dykes probably originated from melting of a spinel-bearing lithospheric mantle metasomatized by subduction-related fluids, with 5-20% crustal contamination, and crystallized at 1100-1135 °C. Both basaltic lavas and diabase dykes have the geochemical characteristics of within-plate basalts. Magmatic zircons from the mafic rocks yield Early Devonian ages (407-403 Ma), postdating the East Kunlun ultrahigh-pressure metamorphism by 19-25 Myr. Comparing our results with the location and timing of the high- and ultrahigh-pressure metamorphic belt, we conclude that the mafic igneous rocks formed in a post-collisional extensional setting. Their generation was associated with both the terminal stages of the Proto-Tethys orogenic belt, (with orogenic collapse promoted by repeated and localized delamination of lithospheric mantle), and early continental rifting related to the evolution of the Paleo-Tethys Ocean to the south. The period of ~426-390 Ma is important for the transition from Proto- to Paleo-Tethys oceans in the East Kunlun Orogen.

Research Data Related to this Submission

There are no linked research data sets for this submission. The following reason is given:
Data will be made available on request

Graphical abstract-R3

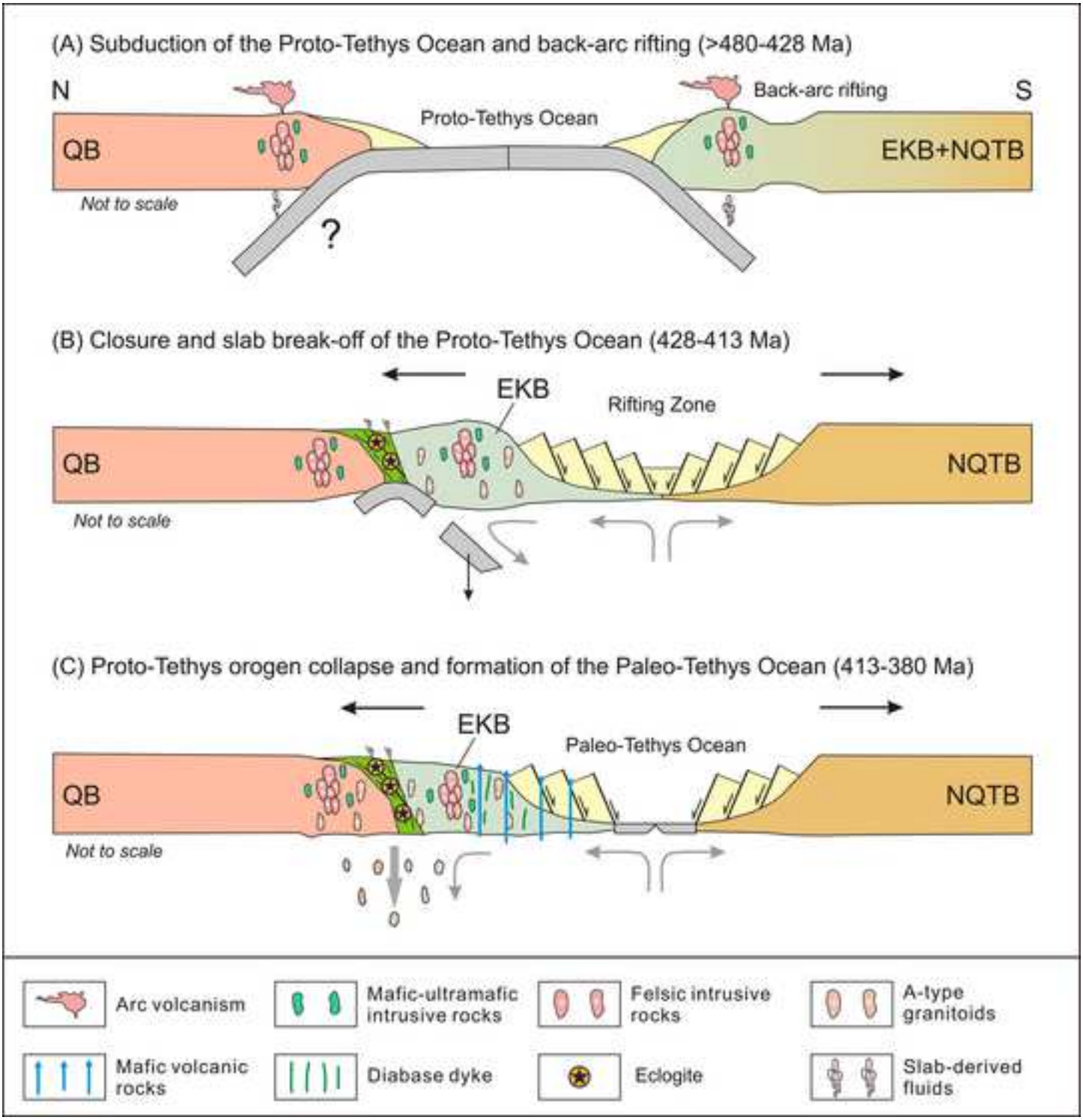

- The Tatuo mafic rocks have geochemical features similar to within-plate basalts.
- The Tatuo mafic rocks (407-403 Ma) formed in a post-collisional extensional setting.
- The period of ~426-390 Ma is important for the transition from the Proto- to Paleo-Tethys oceans.

Early Devonian mafic igneous rocks in the East Kunlun Orogen, NW China: Implications for the transition from the Proto- to Paleo-Tethys oceans

Jinlong Dong [a], Shuguang Song [a*], Li Su [b], Mark B. Allen [c], Yanguang Li [d], Chao Wang [e]

[a] *MOE Key Laboratory of Orogenic Belts and Crustal Evolution, School of Earth and Space Sciences, Peking University, Beijing 100871, China*

[b] *School of Scientific Research and State Key Laboratory of Geological Processes and Mineral Resources, China University of Geosciences, Beijing 100083, China*

[c] *Department of Earth Sciences, University of Durham, Durham DH1 3LE, UK*

[d] *Xi'an Center of Geological Survey, China Geological Survey, Xi'an 710054, China*

[e] *School of Earth Sciences and Resources, China University of Geosciences, Beijing 100083, China*

[*] Corresponding author:

*Shuguang Song

Email: sgsong@pku.edu.cn

Manuscript for *Lithos*

Abstract

The tectonic evolution of the Proto- and Paleo-Tethys oceans had a significant influence on ocean-continent distributions in East Asia in the Phanerozoic, and major implications for continental growth in the region. However, it remains ambiguous when and how the Proto-Tethys Ocean transformed into the Paleo-Tethys Ocean. Here we present petrologic, mineralogical, chronological and geochemical data for Early Devonian mafic igneous rocks, located in the East Kunlun Orogen. The mafic igneous rocks include basaltic lavas and diabase dykes, and are tholeiitic in composition. Geochemical and Sr-Nd isotopic data indicate that the basaltic lavas were derived from melting of a spinel-bearing asthenospheric mantle (E-MORB) at normal mantle potential temperatures (1384-1400 $^{\circ}$C) with negligible (1-4%) crustal contamination. The diabase dykes probably originated from melting of a spinel-bearing lithospheric mantle metasomatized by subduction-related fluids, with 5-20% crustal contamination, and crystallized at 1100-1135 $^{\circ}$C. Both basaltic lavas and diabase dykes have the geochemical characteristics of within-plate basalts. Magmatic zircons from the mafic rocks yield Early Devonian ages (407-403 Ma), postdating the East Kunlun ultrahigh-pressure metamorphism by 19-25 Myr. Comparing our results with the location and timing of the high- and ultrahigh-pressure metamorphic belt, we conclude that the mafic igneous rocks formed in a post-collisional extensional setting. Their generation was associated with both the terminal stages of the Proto-Tethys orogenic belt, (with orogenic collapse promoted by repeated and localized delamination of lithospheric mantle), and early continental rifting related to the

evolution of the Paleo-Tethys Ocean to the south. The period of ~426-390 Ma is important for the transition from Proto- to Paleo-Tethys oceans in the East Kunlun Orogen.

Keywords: Mafic igneous rocks; Post-collisional; Early continental rifting; Proto- and Paleo-Tethys oceans; East Kunlun

1. Introduction

The Proto-Tethys Ocean originally separated continental blocks that are now present across China and SE Asia, from the Qiangtang and Sibumasu blocks to the south and east, to the Tarim and North China blocks to the north (Li et al., 2018). The opening of Proto-Tethys was probably related to the break-up of Rodinia at ~750 Ma, and its closure resulted from the assembly of Gondwana during the Silurian to Early Devonian (Li et al., 2008a; von Raumer and Stampfli, 2008; Zhao et al., 2018a; Song et al., 2018). The Paleo-Tethys Ocean separated the European and Asiatic Hunic terranes and Gondwana (Metcalfe, 2013; Zhao et al., 2018a). Several studies have suggested that the Paleo-Tethys Ocean started to open in the Devonian, and its final closure occurred at ~220 Ma (Jian et al., 2009; Zhai et al., 2011, 2013; Song et al., 2020). The tectonic evolution of the Proto- and Paleo-Tethys oceans clearly played key roles in the assembly of the East Asian blocks in Pangea (Li et al., 2018; Zhao et al., 2018a). However, it is still not well constrained when and how the demise of Proto-Tethys related to the opening of Paleo-Tethys. To address this issue, it is useful to understand the final stages of the Proto-Tethys orogenic belt, and to decipher the early continental rifting related to the opening of Paleo-Tethys.

It is generally accepted that the East Kunlun Orogen (EKO) was a product of the tectonic evolution of the Proto- and Paleo-Tethys oceans (Bian et al., 2004; Chen et al., 2017, 2020; Dong et al., 2018a). Based on high- to ultrahigh-pressure (HP-UHP) metamorphic rocks, recent studies have proposed that the collision event between the East Kunlun and Qaidam blocks could represent the final closure of the Proto-Tethys Ocean (Bi et al., 2018; Song et al., 2018). Therefore, study of the EKO could provide important clues for the late stage evolution of the Proto-Tethys orogenic belt. However, the Middle Silurian to Middle Devonian evolution of the EKO is controversial; both large scale lithospheric delamination and oceanic slab break-off have been proposed as causes of regional extension (Zhang et al., 2014; Zhong et al., 2017; Xin et al., 2018; Chen et al., 2020). Xiong et al. (2014) proposed that the formation of the Paleo-Tethys Ocean started at ~393 Ma, based on within-plate mafic dykes in the EKO, however, the dataset of that study is limited and the early evolution of Paleo-Tethys needs to be re-evaluated.

The geochemistry of mafic igneous rocks can provide important clues for deciphering the nature and composition of their mantle source, and the tectonic setting of melt generation and emplacement (Wilson, 1989; Melluso et al., 2006; Zhu et al., 2008; Lee et al., 2009; Prelević et al., 2012; Song et al., 2015a). In this contribution, we present new petrologic, mineralogical, chronological and geochemical studies for the basaltic lavas and diabase dykes in the EKO. We propose that these mafic igneous rocks formed in a post-collisional setting, consistent with extension, and that they relate to the final collapse of the Proto-Tethys orogenic belt and early continental

rifting related to the opening of the Paleo-Tethys Ocean.

2. Geological background

The EKO is located between the Songpan-Ganzi Terrane and the Qaidam Block on the northeastern margin of the Tibetan Plateau (Fig. 1A). It has dimensions of ~1500 km west-east with a south-north width of ~50-200 km (Fig. 1B). To the south, the Songpan-Ganzi Terrane consists mainly of Late Triassic granitoids (Yuan et al., 2010) and Mesozoic submarine fan and deep marine rocks formed in the Paleo-Tethys Ocean (Ding et al., 2013). To the north, the Qaidam Block predominantly consists of Mesozoic to Cenozoic sedimentary rocks overlying a Precambrian basement (e.g., Xia et al., 2001). The Precambrian basement, primarily exposed at the southern and northern margins of the Qaidam Block, mainly consists of granitic and pelitic gneisses, granitoids, amphibolites and marbles (e.g., Wan et al., 2006).

The EKO is an important tectonic junction linking the Qinling Orogen to the east and the West Kunlun Orogenic Belt to the west (Fig. 1A). It experienced a long and complicated tectonic evolution associated with the Proto- and Paleo-Tethys oceans from the Cambrian to the Triassic (Li et al., 2018; Dong et al., 2018a; Song et al., 2018). The EKO consists of: (1) the A'nyemaqen accretionary belt, (2) extensive granitoids, (3) Precambrian basement and (4) an Early Paleozoic complex (Fig. 1B). In the south of the EKO, the A'nyemaqen accretionary belt (Fig. 1B) consists of tectonic mélanges and ophiolites in a matrix of strongly deformed Permian turbidites (Pei et al., 2018). Based on chronological data, two major episodes of ophiolites, dated at 516-450 Ma and 345-333 Ma, are recognized in the A'nyemaqen accretionary

belt, representing fragments of the ancient Tethys oceans (Bian et al., 2004; Dong et al., 2018a; Pei et al., 2018). In the north of the EKO is the Early Paleozoic complex (Fig. 1B), which primarily consists of eclogites, 537-421 Ma ophiolites, and arc-related igneous rocks (e.g., Yang et al., 1996; Meng et al., 2013; Jiang et al., 2015; Song et al., 2018). The eclogites in the Early Paleozoic complex formed at 432-411 Ma, and occur as interlayers and lenses in a schist matrix (Meng et al., 2013; Qi et al., 2014; Song et al., 2018). The eclogites at Kehete have coesite inclusions and pseudomorphs (Song et al., 2018; Bi et al., 2018), indicating the presence of HP-UHP metamorphism in the EKO. Thus, the Early Paleozoic complex in the EKO is also a HP-UHP metamorphic belt (Fig. 1B). Precambrian basement rocks are widespread in the EKO and they show a wide age range from Paleoproterozoic to Neoproterozoic (He et al., 2016; Song et al., 2018). The granitoids cover an area of more than 48,000 km^2 and they primarily formed in the Early Paleozoic and Triassic (e.g., Chen et al., 2017, 2020; Xin et al., 2018).

The study area is located in the Early Paleozoic complex, at the easternmost part of the EKO (Fig. 1B). The geology of this region includes Precambrian meta-sedimentary rocks, the Early Paleozoic subduction complex, Silurian-Devonian and Mesozoic volcanic-sedimentary strata, Ordovician-Devonian and Permian-Triassic granitoids and ultramafic rocks (Fig. 2A) (BGQP, 1973). The Precambrian meta-sedimentary rocks are composed of dolomitic limestone, marble, sandstone and schist with minor granulite (BGQP, 1973). The Silurian-Devonian volcanic-sedimentary strata (~6.5 km thick in the study area; Fig. 2B) consist mainly

of carbonate, sandstone, slate, pyroclastic rock and volcanic rock (BGQP, 1973). The Mesozoic volcanic-sedimentary strata contain carbonate, conglomerate, sandstone and pyroclastic rock, with minor coal beds. The Silurian-Devonian volcanic-sedimentary strata have fault contacts with the Precambrian meta-sedimentary rocks and Mesozoic volcanic-sedimentary strata (Fig. 2B). The Ordovician-Devonian granitoids consist mainly of syenogranite and granodiorite, showing geochemical features similar to A_2-type granite (Chen et al., 2020).

3. Field relations and petrography

The studied mafic igneous rocks are from the Tatuo area (Fig. 1); sample locations and sampling horizons are shown in Fig. 2A and 2B, respectively. The rocks are basaltic lavas and diabase dykes and their contact relationships cannot be directly observed in the field (Figs. 2A and 3). Basaltic lavas are gray to dark gray in color, and have a massive structure with a thickness of ~70-150 m (Figs. 2B, 3A and 3B). Thin section observations indicate that the basaltic lavas are mainly basalts, with minor amounts of dolerite. Contact relationship between the basalts and dolerites are conformable in the field (Fig. 3B). The basalts are variously altered, but original textures are still present (Fig. 3C and D). They are porphyritic with clinopyroxene (5-10 vol.%) and plagioclase (3-5 vol.%) phenocrysts in a matrix of oriented fine- to micro-grained plagioclase, clinopyroxene, opaque minerals and altered minerals (e.g., chlorite and epidote) (Fig. 3C and D). The dolerites show a fine-grained ophitic texture and are primarily composed of clinopyroxene (35-55 vol.%) and plagioclase (45-60 vol.%) with minor opaques and altered minerals (Fig. 3E).

The two diabase dykes can be found in the study area. These dykes are dark gray in color and possess a massive structure. The dykes are almost vertical, and typical E-W trending. They can be traced for distances of 50-250 m with a width of ~1.5-20 m (Fig. 3F and G). The dykes have intrusive contacts with the Precambrian meta-sedimentary rocks (Fig. 3F and G). There is slight alteration, and ophitic textures (Fig. 3H and I). The compositions are 20-35 vol.% clinopyroxene, 60-75 vol.% plagioclase, and minor altered minerals (Fig. 3H and I). Clinopyroxene grains are irregular to subhedral crystals varying from 0.1 to 1.5 mm in size, and occurring interstially between plagioclase grains (Fig. 3H and I). Clinopyroxene crystals are locally altered to epidote, chlorite and actinolite. Plagioclase grains are euhedral to subhedral laths and vary in size (0.25-2.5 mm) with well-developed polysynthetic twinning (Fig. 3H and I). Some plagioclase grains are mottled in appearance, and altered to kaolin or sericite.

4. Analytical methods

4.1 Mineral chemistry

Mineral analyses for major element oxides, including clinopyroxene and plagioclase, were done on a JEOL JXA-8230 Electron Probe Microanalyzer (EPMA) at the Laboratory of Orogenic Belts and Crustal Evolution of Peking University. Analytical conditions were optimized for standard silicates and oxides at 15 kV accelerating voltage with a 10 nA focused beam current for all the elements. Routine analyses were obtained by counting for 30 s at peak and ~15 s on background. Repeated analysis of natural and synthetic mineral standards yielded precisions better

than ± 2% for most elements.

4.2 Whole-rock major and trace element analyses

Whole-rock major and trace element analysis was performed at the Geological Lab Center of China University of Geosciences, Beijing (CUGB). Whole-rock major element oxides were done using inductively coupled plasma-atomic emission spectroscopy (ICP-OES). The analytical uncertainties are usually less than 1% for most elements with the exception of TiO_2 (~1.5%) and P_2O_5 (~2.0%) based on Chinese national geological standard reference materials GSR-1 and GSR-3, and US Geological Survey rock standards AGV-2 and W-2. Loss on ignition (LOI) was obtained by placing 1000 mg of samples in the furnace at 1000 °C for three hours before being cooled in a desiccator and reweighed. Whole-rock trace elements were determined on an Agilent-7500a inductively coupled plasma-mass spectrometry (ICP-MS). Rock standards AGV-2 (US Geological Survey), and GSR-1, GSR-3, GSR-5 (national geological standard reference materials of China) were used to monitor the analytical accuracy and precision. The analytical accuracy, as indicated by relative difference between measured and recommended values, is better than 5% for most elements, 10-13% for U, Th, Sc, Er, Nb and Cu, and 10-15% for Gd, Ta and Tm. More detailed analytical procedures are presented in Dong et al. (2018b).

4.3 Zircon U-Pb geochronology

Zircons were separated from one dolerite sample (17KL-25) and one diabase dyke sample (18KL-63) by using standard density and magnetic separation techniques and selected by handpicking under a binocular microscope. Cathodoluminescence

(CL) examination was conducted using an FEI QUANTA650 FEG Scanning Electron Microscope (SEM) under conditions of 15 kV/120 nA at MOE Key Laboratory of Orogenic Belt and Crustal Evolution, Peking University.

Measurements of U, Th and Pb in zircons were performed on an Agilent-7700x quadrupole inductively coupled plasma mass spectrometry coupled with a Coherent Geolas Pro laser sampler (LA-ICP-MS) at the Laboratory Center, Xi'an Center of Geological Survey, China. Laser spot size of 25 μm, laser energy density of 6.0 J/cm^2 and a repetition rate of 5 Hz were applied for analysis. Helium was used as a carrier gas to transport the ablated aerosol to the LA-ICP-MS. Each analysis spot comprised about 10 s background measurements and 40 s of sample measurements. National Institute of Standards and Technology 610 glass, zircon standard 91500 and TEM were used for calibration. The software GLITTER 4.4.1 (Macquarie University) was used to process the isotopic ratios and element concentrations of zircon grains. The common Pb correction was made following Andersen (2002). Age calculations and plots of concordia diagrams were done using Isoplot 3.0 (Ludwig, 2003).

4.4 Whole-rock Sr-Nd isotope analyses

Whole-rock Sr-Nd isotope analyses were determined at MOE Key Laboratory of Orogenic Belts and Crustal Evolution, Peking University. About 200 mg of the unknown sample and ~150 mg of the standard sample (BCR-2) were dissolved by using HF+HNO_3 in hermetic Teflon jars and heated at 140 °C for seven days in order to be well dissolved. Separation and purification of the whole-rock Sr-Nd isotope were achieved using conventional cation columns (AG50W and P507). The

whole-rock Sr-Nd isotope analyses were performed on the Micromass Isoprobe multi-collector ICP-MS (MC-ICP-MS). Standard sample BCR-2 was used to evaluate the separation and purification process of Rb, Sr, Sm, and Nd. Mass fractionation corrections for $^{87}Sr/^{86}Sr$ and $^{143}Nd/^{144}Nd$ ratios were normalized to $^{86}Sr/^{88}Sr=0.1194$ and $^{146}Nd/^{144}Nd=0.7219$, respectively.

5. Results

5.1 Mineral chemistry

As the minerals in the basaltic lavas are not fresh (Fig. 3C and D), we only obtain chemical compositions of plagioclase and clinopyroxene from the Tatuo diabase dykes. Representative plagioclase and clinopyroxene compositions of the diabase dykes are given in Table S1 and Table S2, respectively. The plagioclases in the diabase dykes show a wide compositional range and their anorthite contents vary from 36.74 to 71.75 wt.% (Fig. 4A; Table S1). The clinopyroxenes in the diabase dykes are mainly augites, with a formula of $Wo_{37.1-43.7}En_{37.4-45.7}Fs_{13.4-19.7}$ (Fig. 4B; Table S2). Their Mg# [$100\times Mg^{2+}/(Mg^{2+}+Fe^{2+})$] varies from 67 to 78 (Table S2), and is not correlated with Cr_2O_3 (not shown). The clinopyroxenes are characterized by high TiO_2 (0.82-1.62 wt.%), MgO (12.85-16.09 wt.%), low Al_2O_3 (2.88-4.85 wt.%), Cr_2O_3 (0-0.07 wt.%), Na_2O (0.35-0.59 wt.%) and K_2O (0-0.04 wt.%) (Table S2). The clinopyroxene compositions are consistent with those of rift-related igneous rocks (Fig. 4B and C). In the Al_Z versus TiO_2 diagram (Fig. 4C), the clinopyroxene compositions show a rift-related trend.

5.2 Whole-rock major and trace element data

Thirteen basaltic lavas and twelve diabase dykes were analyzed for whole-rock major and trace elements; results are listed in Table S3. Thin section observations indicate that the basaltic lavas and diabase dykes have undergone varying degrees of low-grade greenschist facies metamorphism during post-magmatic processes (Fig. 3C, D, E, H and I). This metamorphism might have modified the contents of fluid-mobile elements (e.g., Ca, K, Na, Rb, Sr and Cs). As a consequence, we have used the immobile elements (e.g., REEs and HFSEs), some major elements (e.g., Si, Fe, Mg, Ti and Al), transitional elements (e.g., Cr, Ni and V) and Nd isotopic data for rock classification and discussion of the petrogenesis. Given the relatively high mobility of Sr and Rb, Sr isotopic data are used and interpreted with caution.

The Tatuo basaltic lavas show varying SiO_2 (47.83-53.31 wt.%, normalized to an anhydrous basis), FeO_T (12.21-16.58 wt.%), relatively high MgO (5.17-8.50 wt.%), medium to high TiO_2 (1.40-2.62 wt.%), low Mg# (40-54), Cr (38-188 ppm) and Ni (47-115 ppm) values (Table S3). The diabase dykes have variable SiO_2 (48.61-55.67 wt.%), high TiO_2 (2.11-3.06 wt.%), FeO_T (10.60-12.52 wt.%), low MgO (3.73-4.83 wt.%), Cr (2-29 ppm) and Ni (4-19 ppm) contents (Table S3). In the Zr/TiO_2 versus Nb/Y diagram (Fig. 5A), all of the samples plot in the sub-alkaline basalt field. In the TiO_2 versus FeO_T/MgO diagram (Fig. 5B), the Tatuo mafic igneous rocks show a tholeiitic trend. The basaltic samples have low ratios of Ti/Y (280-463) and Sm/Yb (1.23-1.82), whereas the diabase dyke samples show low Ti/Y (299-377) and relatively high Sm/Yb (2.13-3.03) (Fig. 5C; Table S3).

The Tatuo basaltic lavas show a large range of total REE contents (47-103 ppm) and possess similar chondrite-normalized REE patterns, with varying LREE enrichment [La_N/Yb_N=1.55-2.89; hereafter, subscript N denotes normalized to the chondrite values of Sun and McDonough (1989)], weak HREE depletion (Gd_N/Yb_N=1.25-1.75) and insignificant Eu anomalies (Eu/Eu*=0.89-0.97) (Fig. 6A). In the primitive mantle-normalized multi-element diagrams (Fig. 6B), the basaltic lavas are characterized by weak "humped" patterns with varying enrichment in U, Ta and REEs and lack negative Nb anomalies. The Tatuo basaltic lavas show geochemical affinities similar to the present-day E-MORB, and their trace element patterns are also similar to those of the low-Ti basalts in Deccan Traps of India (Fig. 6A and B).

The Tatuo diabase dykes have consistent chondrite-normalized REE patterns with obvious LREE enrichment (La_N/Yb_N=7.34-10.50), moderate HREE depletion (Gd_N/Yb_N=1.79-2.26) and discernible negative Eu anomalies (Eu/Eu^*=0.81-0.88) (Fig. 6C). In the primitive mantle-normalized multi-element diagrams (Fig. 6D), the diabase dyke samples display enrichment in Th, U and LREEs with obvious negative Nb-Ta and Ti anomalies. Their geochemical features of trace elements are different from those of OIB, E-MORB, N-MORB and island arc basalts (Fig. 6C and D).

5.3 Zircon U-Pb ages

Two samples, including 17KL-25 (basaltic lava) and 18KL-63 (diabase dyke), were selected for zircon U-Pb age studies. The results of LA-ICP-MS U-Pb zircon analyses are given in Table S4. The cathodoluminescence (CL) images and zircon

U-Pb concordia plots are shown in Fig. 7.

Zircon grains from lava sample 17KL-25, which is dolerite, are mainly subhedral to euhedral, colorless and transparent crystals. They have prismatic shapes (20-120 μm long) with length-to-width ratios of 1.2:1-3:1 (Fig. 7A and B). The CL images indicate that these zircons have straight and wide oscillatory growth bands, which is typical of zircons from mafic igneous rocks (e.g., Song et al., 2015a; Dong et al., 2018b). Zircons from sample 17KL-25 have variable concentrations of U (120-874 ppm) and Th (66-824 ppm), with high Th/U ratios that vary from 0.33 to 1.08 (average of 0.59) (Table S4). Five analyzed spots with Th/U ratios of 0.46-0.68 yield relatively old apparent $^{206}Pb/^{238}U$ ages of 452-431 Ma, with a weighted mean of 439.6 ± 3.5 Ma (MSWD=0.17; Fig. 7A). We interpret that these zircons are xenocrysts and the age of ~440 Ma is consistent with the timing of arc magmatism in the EKO (e.g., Jiang et al., 2015). Sixteen analyzed spots yield apparent $^{206}Pb/^{238}U$ ages of 425-395 Ma with a weighted mean of 407.0 ± 3.9 Ma (MSWD=2.3; Fig. 7B), which is interpreted as the eruption time of the Tatuo basaltic lavas.

Most zircon grains from the diabase dyke sample (18KL-63) are sub-rounded, rounded and oval in morphology and show equant to long prismatic shapes (20-150 μm long) with length-to-width ratios of 1:1-3.5:1 (Fig. 7C). CL images indicate that these zircons are mainly light to dark grey with clear oscillatory zoning. Some zircons have inherited cores and overgrown rims (Fig. 7C). Twelve analyses were conducted on these zircons and yield old apparent $^{206}Pb/^{238}U$ ages of 2447-467 Ma (Table S4), which are likely to be xenocrysts. Three zircon grains are subhedral to euhedral, and

stubby (30-60 μm long with length-to-width ratios of 1.2:1-1.8:1) (Fig. 7C). CL images show that the three zircon grains have straight and wide oscillatory growth bands (Fig. 7C), typical of zircons derived from mafic magmas. The three zircons show various concentrations of U (546-727 ppm) and Th (283-458 ppm) with high Th/U ratios varying from 0.43 to 0.63 (Table S4). They yield the youngest apparent $^{206}Pb/^{238}U$ ages of 406-400 Ma with a weighted mean of 402.7 ± 4.8 Ma (MSWD=0.58; Fig. 7D). Thus, we interpret the age of ~403 Ma to represent the emplacement timing of the diabase dykes, which is coeval, within error, with the basaltic lavas.

5.4 Whole-rock Sr-Nd isotope data

Eight basaltic lava and four diabase dyke samples were analyzed for whole-rock Sr-Nd isotopic compositions. The results are listed in Table S5 and plots of $\varepsilon_{Nd}(t)$ versus $I_{Sr}(t)$ are displayed in Fig. 8A. Initial isotopic ratios of basaltic lavas and diabase dykes were calculated at 407 Ma and 403 Ma, respectively. Both the basaltic lava and diabase dyke samples show relatively wide ranges of the whole-rock Sr-Nd isotopic compositions (Table S5; Fig. 8A). The basaltic lavas show weakly to moderately positive $\varepsilon_{Nd}(t)$ values (+1.27 to +4.65) with initial $^{87}Sr/^{86}Sr$ ratios ranging from 0.70359 to 0.71041. Several basaltic samples (11KL-02, 05, 39 and 41 and 17KL-25) exhibit a trend towards high Sr isotope values at a constant $\varepsilon_{Nd}(t)$ value, which is likely to be due to alteration by hydrothermal fluids (Fig. 8A). The diabase dyke samples have moderately negative $\varepsilon_{Nd}(t)$ values (-4.54 to -1.88) and relatively high initial $^{87}Sr/^{86}Sr$ ratios ranging between 0.70886 to 0.71513. Notably, the diabase

dyke samples do not show a trend parallel to abscissa axis with increasing $I_{Sr}(t)$, indicating that late alteration could be insignificant (Fig. 8A). Two-stage depleted mantle model ages (T_{DM2}) of the basaltic lavas vary from 769 Ma to 1044 Ma, whereas the T_{DM2} ages of the diabase dykes are much older, in the range of 1298-1513 Ma (Table S5). In the $\varepsilon_{Nd}(t)$ versus Mg# diagram (Fig. 8B), the basaltic lavas show a moderately segmented trend, suggesting significant fractional crystallization and limited crustal contamination during magma evolution and migration. The obvious negative correlations between $\varepsilon_{Nd}(t)$ and Mg# (Fig. 8B) indicate that the diabase dyke samples were strongly affected by crustal contamination.

6. Discussion

6.1 Petrogenesis

6.1.1 Fractional crystallization

In general, primary magmas generated from mantle peridotites should have high Cr (300-500 ppm), Ni (300-400 ppm) and Mg# values (68-76) (Frey et al., 1978; Wilson, 1989). All the Tatuo mafic igneous rocks are characterized by low Cr (2-188 ppm), Ni (4-115 ppm) and Mg# values (37-54) (Table S3), indicating fractional crystallization of olivine, pyroxene and spinel during the magmatic evolution. For the basaltic lavas, the possible fractional crystallization can also be observed in the flat trend of the $\varepsilon_{Nd}(t)$ versus Mg# diagram (Fig. 8B). Negative correlations of MgO and FeO_T with SiO_2 (Fig. 9A and B) imply that the primary magmas of both the basaltic lavas and diabase dykes experienced fractional crystallization of mafic minerals. For the basaltic lavas, the relatively poor correlation between Al_2O_3 and SiO_2 (r=0.55; Fig.

9C) implies limited fractionation of plagioclase, consistent with the insignificant Eu anomalies (Eu/Eu*=0.89-0.97) (Fig. 6A). In contrast, for the diabase dykes, the strongly negative correlation of Al_2O_3 with SiO_2 (r=0.94; Fig. 9C) indicates possible plagioclase crystallization, supported by the negative Eu anomalies (Eu/Eu^*=0.81-0.88) (Fig. 6C). In addition, Fe-Ti oxide crystallization plays an important role in the evolution of the basaltic lavas, which is suggested by the negative correlation between TiO_2 and MgO (Fig. 9D). For the diabase dykes, fractionation of Fe-Ti oxides can be discounted, due to the absence of a negative correlation between TiO_2 and MgO (Fig. 9D). The obvious correlations of Ni and V with Cr (Fig. 9E and F) indicate that primary magmas of both the basaltic lavas and diabase dykes underwent significant fractionation of clinopyroxene. Hornblende crystallization can be discounted for both the basaltic lavas and diabase dykes, because of the absence of MREE depletion (Fig. 6A and C). In summary, the basaltic lavas underwent fractionation of clinopyroxene, Fe-Ti oxide and minor plagioclase, whereas the diabase dykes likely experienced fractionation of clinopyroxene and plagioclase.

6.1.2 Crustal contamination

It is important to evaluate the potential role of crustal contamination in the Tatuo mafic igneous rocks. Contamination appears to be limited for the Tatuo basaltic lavas because: (1) crustal contamination could give rise to negative Nb-Ta and positive Zr-Hf anomalies (Zhou et al., 2007), but the basaltic lavas are characterized by slightly negative to positive Nb anomalies [Nb_{PM}/La_{PM}=0.70-1.01; hereafter, subscript

PM denotes normalized to the primary mantle values of Sun and McDonough (1989)], positive Ta anomalies (Ta_{PM}/Th_{PM}=0.93-2.59) and slightly negative Zr-Hf anomalies (Fig. 6B); (2) in the Th/Yb versus Nb/Yb diagram (Fig. 10A), all the basaltic samples plot within the MORB-OIB array; (3) in the Nb/Th versus Nb/La diagram (Fig. 10B), the basaltic samples do not show a crustal contamination trend; and (4) the presence of moderately segmented trends between $\varepsilon_{Nd}(t)$ and Mg# (Fig. 8B) for the basaltic lavas also confirms the limited effect of crustal contamination.

By comparison, the influence of crustal contamination is very significant for the Tatuo diabase dykes, due to the presence of the prominent negative correlation between $\varepsilon_{Nd}(t)$ and Mg# (Fig. 8B). Crustal contamination can also be inferred by the abundant zircons captured by the mafic dykes (see above). It is worth noting that the upper continental crust is more enriched in Th compared to lower and middle continental crusts (Rudnick and Gao, 2003), indicating that the crustal contaminant for the Tatuo diabase dykes could be derived from the upper continental crust.

6.1.3 Mantle source

Mafic igneous rocks were generally derived from either lithospheric mantle or asthenospheric mantle (George and Rogers, 2002; Dong et al., 2019). Rocks derived from the lithospheric mantle are characterized by low $\varepsilon_{Nd}(t)$ values and high initial $^{87}Sr/^{86}Sr$ ratios, whereas those from the asthenospheric mantle have depleted signatures in isotopes (e.g., Dong et al., 2019). In our study, although some basaltic samples (17KL-25 and 11KL-02, 05, 39 and 41) show relatively high initial $^{87}Sr/^{86}Sr$ ratios due to the subsequent alteration (Fig. 8A), all the basaltic lavas are

393 characterized by high $\varepsilon_{Nd}(t)$ (+1.27 to +4.65) and slightly enriched in LREEs and
394 HFSEs with insignificant crustal contamination (Figs. 6A-B and 8B). These pieces of
395 evidence indicate that the basaltic lavas could be derived from the asthenospheric
396 mantle and show geochemical affinities with E-MORB (Hofmann, 1997). In the
397 Th/Yb versus Nb/Yb and Nb/Zr versus Th/Zr diagrams (Fig. 10A and C) the entire
398 basaltic sample set plots within the MORB-OIB array, and close to E-MORB.

399 By comparison, the diabase dyke samples are characterized by negative $\varepsilon_{Nd}(t)$
400 (-4.54 to -1.88) and high initial $^{87}Sr/^{86}Sr$ (0.70886 to 0.71513) with T_{DM2} ages of
401 1298-1513 Ma (Table S5), implying that they originated from the lithospheric mantle.
402 Moreover, the Zr/Nb (15.90-31.76), Th/Ta (10.41-15.30) and La/Nb (3.26-4.04)
403 values of the diabase dykes are far higher than those of MORB (Sun and McDonough,
404 1989), further confirming their derivation from the lithospheric mantle. In general, the
405 continental crust has negative Nb/Nb* anomalies (0.23-0.55)
406 [$Nb/Nb^{*}=Nb_{PM}/(Th_{PM}\times La_{PM})^{1/2}$] and low Nb/La ratios (0.39-0.63) with positive Zr-Hf
407 anomalies (Rudnick and Gao, 2003). In the Tatuo case, the diabase dyke samples
408 show much lower Nb/Nb* (0.18-0.21) and Nb/La (0.25-0.29) values than those of the
409 continental crust, indicating that their mantle source could be more complicated. For
410 the diabase dykes, the negative Zr-Hf anomalies (Fig. 6D), especially for sample
411 17KL-72 and 18KL-63, indicate that their mantle source could have been
412 metasomatized by subduction-related fluids/melts. The inference could be
413 demonstrated in the Th/Yb versus Nb/Yb and Nb/Th versus Nb/La diagrams (Fig.
414 10A and B): the diabase dykes plot outside of the MORB-OIB array and show very

415 limited variation ranges, indicating that they inherit the features of a mantle source
416 previously metasomatized by subduction-related fluids/melts. In the Nb/Zr versus
417 Th/Zr diagram (Fig. 10C), the diabase dyke samples significantly deviate from the
418 MORB-OIB array, reflecting the influence of slab-derived fluids.

419 To further determine the type of mantle source and effect of crustal
420 contamination for the Tatuo mafic igneous rocks, we utilize the simple binary mixing
421 model proposed by DePaolo (1981) and Zhou et al. (2007). In this modeling, we make
422 the following assumptions: (1) the Wanbaogou sandstone from the EKO represents
423 the crustal end member; (2) the Xiarihamu mafic-ultramafic intrusion in the EKO
424 represents the subcontinental lithospheric mantle source; and (3) the E-MORB glasses
425 from the Gakkel Ridge proposed by Mühe et al. (1997) represents the asthenospheric
426 mantle source. As shown in Fig. 10D, the calculation results indicate that the basaltic
427 lavas were derived from asthenospheric mantle (E-MORB) with insignificant (<4%)
428 crustal contamination, whereas the diabase dykes were originated from subcontinental
429 lithospheric mantle with various degrees (5-20%) of crustal contamination.

430 Ratios of REEs in basaltic lavas are used to distinguish the nature of the mantle
431 source and roughly estimate the degree of melting (e.g., George and Rogers, 2002). In
432 this study, we use the method suggested by George and Rogers (2002) to determine
433 the nature of mantle source for the Tatuo mafic igneous rocks. As shown in Fig. 11A,
434 the basaltic lavas have low ratios of La/Yb (2.16-4.03) and Tb/Yb (0.25-0.33),
435 indicating that they were possibly produced by 5-7% partial melting of spinel-bearing
436 mantle source. However, as mentioned above, the diabase dykes have been

437 significantly affected by crustal contamination and slab-derived fluids. In those
438 processes, LREEs might be significantly changed, but HREEs could be inactive (e.g.,
439 Green, 2006). Thus, the low ratios of Tb/Yb (0.31-0.38) from the diabase dykes
440 indicate a spinel-bearing mantle source (Fig. 11A).

441 6.1.4 Mantle/crystallization temperature

442 Among the basaltic lavas, samples 17KL-21, 22 and 25 are the least-evolved
443 with the highest MgO (8.29-8.50 wt.%) and Mg# (~54). For these samples, we invoke
444 the method of Lee et al. (2009) to estimate the main oxide components for the
445 primitive magmas and the mantle potential temperature (T_p). The calculation results
446 show that the primitive magmas are high-Mg basaltic compositions with 48.08-50.45
447 wt.% SiO_2, 9.36-9.63 wt.% FeO_T and 12.74-13.21 wt.% MgO. The resulting T_p varies
448 from 1384 $^{\circ}$C to 1400 $^{\circ}$C. The mantle potential temperatures are very close to those of
449 the typical upper mantle (1350 $^{\circ}$C) (Davies, 2009).

450 For the diabase dykes, on account of the significant effects of crustal
451 contamination and slab-derived fluids (see above), we use clinopyroxene-only
452 thermometers proposed by Nimis and Taylor (2000) to give an approximate estimate
453 of the crystallization temperature. In the calculation, we adopt the hypothesis that the
454 high-Mg (Mg#>75) clinopyroxenes within the diabase dykes could be in equilibrium
455 with the primitive magmas. Applying this method, the calculated crystallization
456 temperature is between 1100 $^{\circ}$C and 1135 $^{\circ}$C for the Tatuo diabase dykes.

457 **6.2 Tectonic setting of the EKO during ~426-390 Ma**

458 Mafic igneous rocks can occur in multiple tectonic settings, such as mid-ocean

ridges, subduction zones and within-plate regimes (e.g., Wilson, 1989). The Tatuo mafic igneous rocks exhibit high TiO_2 (1.40-3.06 wt.%), Zr (70-282 ppm), V (179-459 ppm), Zr/Y (3.0-6.0) and Zr/Sm (23.3-30.0), similar to those of the within-plate mafic rocks (Wilson, 1989; Li et al., 2008b). In the V versus Ti/1000 diagram (Fig. 11B), the mafic rock samples mainly plot in the continental flood basalts (CFB) field. The affinities of within-plate basalts can also be observed by trace element patterns and clinopyroxene compositions (Figs. 4B, 4C and 6). However, the calculated mantle and crystallization temperatures (1100-1400 $^{\circ}$C) for the Tatuo mafic igneous rocks are far less than those of the Hawaiian picrites (1500-1600 $^{\circ}$C) (Lee et al., 2009), indicating that they are not associated with a mantle-plume event.

Several studies have proposed that the EKO records the evolution of the Proto-Tethys Ocean from early Cambrian subduction, to oceanic closure, to continental collision (e.g., Qi et al., 2014; Dong et al., 2018a; Song et al., 2018; Bi et al., 2018). The UHP metamorphic ages in the EKO are mainly clustered at 428-426 Ma (Song et al., 2018), which represents the final closure of the Proto-Tethys Ocean (Song et al., 2018; Bi et al., 2018) and are before the formation of the Tatuo mafic igneous rocks (407-403 Ma). Given these timings, the Tatuo mafic igneous rocks could have formed in a syn- or post-collisional setting. However, syn-collisional magmatic rocks are mainly originated from both oceanic and continental crust with rare mantle-derived components (e.g., Song et al., 2015b), such as the Xitieshan syn-collisional granites (Zhao et al., 2017). We therefore propose that the Tatuo mafic igneous rocks could form in a post-collisional extensional setting. Recent studies have

showed that ~412-392 Ma mafic igneous rocks with within-plate basalt features and ~426-390 Ma A_2-type granitoids are distributed in other places in the EKO, such as Weibao, Haxiya and Wulonggou, and also interpret a post-collisional extensional setting (Yang et al., 2014; Zhong et al., 2017; Xin et al., 2018; Chen et al., 2020). Taking the spatial and temporal relations and tectonic settings of these ~426-390 Ma igneous rocks into consideration, we suggest that the whole EKO was in the post-collisional extensional setting during ~426-390 Ma.

6.3 Geodynamic Implications

In general, lithospheric mantle is relatively cold, and only melts to generate mafic magma if there is involvement of an additional heat source. For most post-collisional settings, the asthenospheric mantle is considered as the potential heat source (Zhao et al., 2018b). It is generally accepted that involvement of the asthenospheric mantle in melting in post-collisional settings results from one or more of the following: slab break-off, wholesale convective removal of the lithosphere, lithosphere delamination, and small-scale sublithospheric convection (e.g., Bird, 1979; Houseman et al., 1981; von Blanckenburg and Davies, 1995; Kaislaniemi et al., 2014; Zhu et al., 2015; Zhao et al., 2018b). In our case, any proposed tectono-magmatic model for the Tatuo mafic igneous rocks in the EKO must be able to explain the following features: (1) the volume is relatively small; (2) the mantle source for the basaltic lavas was the asthenospheric mantle; (3) the mantle source for the diabase dykes could be the lithospheric mantle metasomatized by slab-derived fluids; and (4) the mafic igneous rocks show within-plate geochemical affinities. In addition, the

503 tectono-magmatic model must also be responsible for the following observations: (1)
504 as shown in Fig. 11C, peak magmatism in the EKO occurred at ~423 Ma, postdating
505 the UHP metamorphism with a very short time interval (~3-5 Myr); (2) the A_2-type
506 granitoids at the magmatic peak period could possibly be created with input of
507 asthenosphere-derived components (Fig. 11D); and (3) the mafic igneous rocks in the
508 EKO, dated at ~412-392 Ma (e.g., Yang et al., 2014; Xiong et al., 2014; Zhong et al.,
509 2017), are scattered and have small volumes, such as the Weibao, Haxiya, Yuejinshan
510 and Tatuo examples.

511 Slab break-off occurs due to the contrasting buoyancy and tensile forces,
512 between the resistant, buoyant, continental lithosphere and subducting oceanic
513 lithosphere (von Blanckenburg and Davies, 1995). The model predicts a linear zone of
514 magmatism along the orogenic belt, occurring ~1-10 Myr after continental collision
515 (e.g., von Blanckenburg and Davies, 1995; Macera et al., 2008). In this model, the
516 magmatism is variable in composition, and includes bimodal volcanic rocks, A_2-type
517 felsic rocks and within-plate mafic rocks (e.g., von Blanckenburg and Davies; Zhu et
518 al., 2015). The model is reasonable to explain two of the observations of the
519 post-collisional magmatism in the EKO: (1) peak magmatism postdated the UHP
520 metamorphism by ~3-5 Myr (Fig. 11C), and (2) the possible input of
521 asthenosphere-derived components started at ~423 Ma, synchronous with peak
522 magmatism (Fig. 11D). However, the slab break-off model does not explain the
523 temporally- and spatially-scattered style and volumes of the mafic magmatism in the
524 EKO, dated at ~412-392 Ma (e.g., Yang et al., 2014; Xiong et al., 2014; Zhong et al.,

525 2017). In addition, the model does not explain the relatively long-term (~20 Myr)
526 mafic within-plate magmatism in the EKO.

527 Convective removal of the lithosphere involves a regional detachment of the
528 lower lithosphere (Houseman et al., 1981; Morency et al., 2002). The model has been
529 used to explain the potassic and ultrapotassic rocks of orogenic plateaux (e.g., Song et
530 al., 2015b), such as the 15.6-4.5 Ma volcanic rocks in Southwestern Anatolia, Turkey
531 (Prelević et al., 2012). However, the lack of extensive potassic and ultrapotassic rocks
532 in the EKO argues against the model of wholesale convective removal of the
533 lithosphere.

534 The delamination model predicts that the lithospheric mantle peels away with or
535 without portion of the eclogitic lower crust, resulting in the upwelling of heated
536 asthenosphere and crust-mantle interaction (Bird, 1979). Lithospheric delamination
537 would give rise to extensive lower and middle crustal melting as well as formation of
538 massive amounts of asthenosphere-derived rocks. However, the lack of lower
539 crust-derived rocks, such as adakites and tonalites, and large-scale
540 asthenosphere-derived mafic igneous rocks rule out the delamination model for the
541 EKO.

542 The small-scale sublithospheric convection model predicts that previous
543 subduction resulted in wetting of the lower lithosphere and upper asthenosphere and a
544 decrease in mantle viscosity, which gave rise to repeated and localized delamination
545 of the lowermost lithosphere and upwelling of asthenosphere (Kaislaniemi et al., 2014;
546 Kheirkhah et al., 2015). Results from numerical modeling indicate that the small-scale

lithospheric delamination could not be observed by seismic tomography at depths far shallower than 100 km (Kaislaniemi et al., 2014). In the model, the igneous rocks may have geochemical features similar to within-plate rocks (e.g., Kheirkhah et al., 2015). The model can explain long-term magmatic activities which display no clear patterns in space and time (Kaislaniemi et al., 2014). The model is reasonable to explain the spatially and temporally scattered pattern of the mafic igneous rocks dated at ~412-392 Ma in the EKO (e.g., Yang et al., 2014; Xiong et al., 2014; Zhong et al., 2017). In summary, we propose that the final collapse of the Proto-Tethys orogenic belt was induced by the repeated and localized delamination of lithospheric mantle during ~412-390 Ma.

There is commonly a time lag of >30-40 Myr between the post-collisional magmatism and HP-UHP metamorphism in typical collisional orogenic belts worldwide (e.g., Song et al., 2015b). However, the time lag between the post-collisional magmatism and UHP metamorphism in the EKO is relatively short and less than 36 Myr, which is different from the typical collisional orogenic belts around the world. These pieces of evidence indicate that the EKO is distinctive. Several studies have documented that the seafloor spreading of the Paleo-Tethys Ocean started at ~383-333 Ma in the northern and eastern Tibetan plateau, with data from regions such as Qiangtang, East Kunlun, Jinshajiang and Ailaoshan (e.g., Jian et al., 2009; Zhai et al., 2013; Pei et al., 2018). It is generally accepted that early continental rifting related to the opening of the Paleo-Tethys Ocean occurred at ~443-401 Ma, based on low-Ti-CFB xenoliths in the Jinshajiang mélange (Jian et al.,

569 2009). This age is almost synchronous with the formation of the post-collisional
570 igneous rocks (~426-390 Ma) in the EKO. Therefore, we propose that the ~426-390
571 Ma post-collisional igneous rocks in the EKO are a magmatic response to the early
572 continental rifting related to the formation of the Paleo-Tethys Ocean.

573 Previous studies have proposed that mantle plumes or back-arc rifting plays a
574 vital role in the opening of ocean basins (e.g., Stampfli and Borel, 2002; Zhang et al.,
575 2018). In the case of the EKO, back-arc rifting could be responsible for the formation
576 of the Paleo-Tethys Ocean, because: (1) the large-scale alkaline flood basalts are
577 absent in the EKO; (2) the calculated mantle/crystallization temperatures for the Tatuo
578 mafic igneous rocks are relatively low (1100-1400 $^{\circ}$C; see above), implying that the
579 EKO did not possess thermal anomalies at this time (Li et al., 2008b; Lee et al., 2009);
580 and (3) arc-related igneous rocks, dated at ~480-438 Ma (Liu et al., 2013; Jiang et al.,
581 2015; Dong et al., 2018), are common in the EKO. Given the distribution of Early
582 Paleozoic arc rocks and results of structural analyses (Liu et al., 2013; Jiang et al.,
583 2015; Li et al., 2018; Dong et al., 2018a), we further suggest that the back-arc rifting
584 could have result from the southwards subduction of the Proto-Tethys Ocean. These
585 pieces of evidence indicate that the ~426-390 Ma post-collisional igneous rocks in the
586 EKO recorded the transition from the Proto- to Paleo-Tethys oceans.

587 We propose the following geodynamic model for the full evolution of the EKO
588 (Fig. 12). During the Proto-Tethys subduction stage, the lithospheric mantle was
589 metasomatized by the slab-derived fluids, accompanying the formation of arc-related
590 igneous rocks (e.g., Jiang et al., 2015; Dong et al., 2018a), and subduction beneath the

East Kunlun-North Qiangtang Block led to back-arc rifting (Fig. 12A). As the subduction proceeded, the Proto-Tethys oceanic slab reached up to UHP eclogite facies during ~428-426 Ma (Song et al., 2018), marking the final closure of the Proto-Tethys Ocean and onset of continental collision (Fig. 12B). Slab break-off of the Proto-Tethys oceanic plate occurred at ~423 Ma, shortly after continental collision (Fig. 12B). During this stage, uprising asthenosphere would have impinged upon the lithospheric mantle of the overriding slab, accompanying exhumation of HP-UHP rocks and rapid orogenic uplift (Fig. 12B), which is evidenced by the 423-400 Ma deposition of molasse sediments in the EKO (Lu et al., 2010). In addition, conductive heating would have resulted in the partial melting of continental crust, generating 426-418 Ma A_2-type granitoids (Xin et al., 2018; Chen et al., 2020) (Fig. 12B). Finally, the EKO collapsed by the repeated and localized delamination of the lower lithosphere during ~412-390 Ma, which could be facilitated by the continental rifting. The Paleo-Tethys Ocean has started to grow since ~383 Ma (Fig. 12C). During this process, upwelling of asthenosphere led to the formation of mafic igneous rocks, which show within-plate geochemical features and have no clear patterns in time and space (e.g., Yang et al., 2014; Xiong et al., 2014; Zhong et al., 2017).

7. Conclusions

The Tatuo mafic igneous rocks are mainly composed of basaltic lavas and diabase dykes. Geochemical and isotopic data suggest that the basaltic lavas could be originated from melting of a spinel-bearing asthenosphere (E-MORB) with insignificant (<4%) crustal contamination, whereas the diabase dykes were likely

derived from a spinel-bearing lithospheric mantle metasomatized by slab-derived fluids with 5-20% crustal contamination. The geochemical features of the Tatuo mafic igneous rocks are similar to those of within-plate basalts. Magmatic zircons indicate that the basaltic lavas and diabase dykes formed at 407.0 ± 3.9 Ma and 402.7 ± 4.8 Ma, respectively. The formation of the Tatuo mafic igneous rocks were related to both the final collapse of the Proto-Tethys orogenic belt, induced by repeated and localized delamination of lithospheric mantle, and continental rifting related to the formation of the Paleo-Tethys Ocean.

Acknowledgements

We thank Lebing Fu, two anonymous reviewers and Editor-in-chief Xian-Hua Li for their detailed and constructive comments, which greatly improved the quality of the paper. We thank the members of the Element Geochemical Lab, China University of Geosciences, Beijing (CUGB), for their help with major and trace element analyses; Xiaoli Li for his help with electron probe analyses; Mengqi Jin for her help with zircon LA-ICP-MS U-Pb dating; Wenping Zhu and Guibing Zhang for their help with whole-rock Sr-Nd isotopic analyses. We are also grateful to Liming Yang, Hengzhe Bi and Fan He for their field assistance. This work was financially supported by the National Natural Science Foundation of China (grants 91955202, 41572040).

References

Andersen, T., 2002. Correction of common lead in U-Pb analyses that do not report ^{204}Pb. Chemical Geology 192, 59–79.

Bi, H.Z., Song, S.G., Dong, J.L., Yang, L.M., Qi, S.S., Allen, M.B., 2018. First

635 discovery of coesite in eclogite from East Kunlun, northwest China. Science
636 Bulletin, 63: 1536–1538.
637 Bian, Q.T., Li, D.H., Pospelov, I., Yin, L.M., Li, H.S., Zhao, D.S., Chang, C.F., Luo,
638 X.Q., Gao, S.L., Astrakhantsev, O., Chamov, N., 2004. Age, geochemistry and
639 tectonic setting of Buqingshan ophiolites, North Qinghai-Tibet Plateau, China.
640 Journal of Asian Earth Sciences 23, 577–596.
641 Bird, P., 1979. Continental delamination and the Colorado Plateau. Journal of
642 Geophysical Research: Solid Earth 84, 7561–7571.
643 Bureau of Geology, Qinghai Province (BGQP), 1973. Geological Map of Jialuhe,
644 Qinghai Province, Scale 1: 200,000 (in Chinese).
645 Chen, J.J., Fu, L.B., Wei, J.H., Selby, D., Zhang, D.H., Zhou, H.Z., Zhao, X., Liu, Y.,
646 2020. Proto-Tethys magmatic evolution along northern Gondwana: Insights from
647 Late Silurian-Middle Devonian A-type magmatism, East Kunlun Orogen,
648 Northern Tibetan Plateau, China. Lithos 356–357, 105304.
649 Chen, J.J., Wei, J.H., Fu, L.B., Li, H., Zhou, H.Z., Zhao, X., Zhan, X.F., Tan, J., 2017.
650 Multiple sources of the early Mesozoic Gouli batholith, Eastern Kunlun
651 Orogenic Belt, northern Tibetan Plateau: linking continental crustal growth with
652 oceanic subduction. Lithos 292–293, 161–178.
653 Dong, J.L., Song, S.G., Su, L., Li, Y.G., Yang, L.M., Wang, C., Xu, B., 2019. Onset of
654 the North-South Gravity Lineament, NE China: constraints of late Jurassic
655 bimodal volcanic rocks. Lithos 334–335, 58–68.
656 Dong, Y.P., He, D.F., Sun, S.S., Liu, X.M., Zhou, X.H., Zhang, F.F., Yang, Z., Cheng,

B., Zhao, G.C., Li, J.H., 2018a. Subduction and accretionary tectonics of the East Kunlun Orogen, western segment of the Central China Orogenic System. Earth-Science Reviews 186, 231–261.

Dong, J.L., Song, S.G., Wang, M.M., Allen, M.B., Su, L., Wang, C., Yang, L.M., Xu, B., 2018b. Alaskan-type Kedanshan intrusion (central Inner Mongolia, China): Superimposed subduction between the Mongol-Okhotsk and Paleo-Pacific oceans in the Jurassic. Journal of Asian Earth Sciences 167, 68–81.

Ding, L., Yang, D., Cai, F.L., Pullen, A., Kapp, P., Gehrels, G.E., Zhang, L.Y., Zhang, Q.H., Lai, Q.Z., Yue, Y.H., Shi, R.D., 2013. Provenance analysis of the Mesozoic Hoh-Xil–Songpan-Ganzi turbidites in northern Tibet: implications for the tectonic evolution of the eastern Paleo-Tethys Ocean. Tectonics 32, 1–15.

Davies, G.F., 2009. Effect of plate bending on the Urey ratio and the thermal evolution of the mantle. Earth and Planetary Science Letters 287, 513–518.

DePaolo, D.J., 1981. A neodymium and strontium isotopic study of the Mesozoic calcalkaline granitic batholiths of the Sierra-Nevada and Peninsular Ranges, California. Journal of Geophysical Research 86, 470–488.

Frey, F.A., Green, D.H., Roy, S.D., 1978. Integrated models of basalt petrogenesis: a study of quartz tholeiites to olivine melilitites from South Eastern Australia utilizing geochemical and experimental petrological data. Journal of Petrology 19, 463–513.

Green, N.L., 2006. Influence of slab thermal structure on basalt source regions and melting conditions: REE and HFSE constraints form the Garibaldi volcanic belt,

679 northern Cascadia subduction system. Lithos 87, 23–49.
680 George, R., Turner, S., Hawkesworth, C., Morris, J., Nye, C., Ryan, J., Zheng, S.-H.,
681 2003. Melting processes and fluid and sediment transport rates along the Alaska–
682 Aleutian arc from an integrated U-Th-Ra-Be isotope study. Journal of
683 Geophysical Research. doi:10.1029/2002JB001916.
684 George, R., Rogers, N., 2002. Plume dynamics beneath the African plate inferred
685 from the geochemistry of the Tertiary basalts of southern Ethiopia. Contributions
686 to Mineralogy and Petrology 144, 286–304.
687 He, D.F., Dong, Y.P., Liu, X.M., Yang, Z., Sun, S.S., Cheng, B., Li, W., 2016.
688 Tectono-thermal events in East Kunlun, Northern Tibetan Plateau: evidence from
689 zircon U-Pb geochronology. Gondwana Research 30, 179–190.
690 Hofmann, A., 1997. Mantle geochemistry: the message from oceanic volcanism.
691 Nature 389, 219–229.
692 Houseman, G., McKenzie, D., Molnar, P., 1981. Convective instability of a thickened
693 boundary layer and its relevance for the thermal evolution of continental
694 convergent belts. Journal of Geophysical Research 86, 6115–6132.
695 Jiang, C.Y., Ling, J.L., Zhou, W., Du, W., Wang, Z.X., Fan, Y.Z., Song, Y.F., Song,
696 Z.B., 2015. Petrogenesis of the Xiarihamu Ni bearing layered mafic-ultramafic
697 intrusion, East Kunlun: implications for its extensional island arc environment.
698 Acta Petrologica Sinica 31(4), 1117–1136 (in Chinese with English abstract).
699 Jian, P., Liu, D.Y., Kröner, A., Zhang, Q., Wang, Y.Z., Sun, X.M., Zhang, W., 2009.
700 Devonian to Permian plate tectonic cycle of the Paleo-Tethys Orogen in

701 southwest China (II): insights from zircon ages of ophiolites, arc/back-arc
702 assemblages and withinplate igneous rocks and generation of the Emeishan CFB
703 province. Lithos 113, 767–784.
704 Kaislaniemi, L., van Hunen, J., Allen, M.B., Neill, I., 2014. Sublithospheric
705 small-scale convection—A mechanism for collision zone magmatism. Geology
706 42, 291–294.
707 Kheirkhah, M., Neill, I., Allen, M.B., 2015. Petrogenesis of OIB-like basaltic volcanic
708 rocks in a continental collision zone: Late Cenozoic magmatism of Eastern Iran.
709 Journal of Asian Earth Sciences 106, 19–33.
710 Lee, C.T.A., Luffi, P., Plank, T., Dalton, H., Leeman, W.P., 2009. Constraints on the
711 depths and temperatures of basaltic magma generation on Earth and other
712 terrestrial planets using new thermobarometers for mafic magmas. Earth and
713 Planetary Science Letters 279, 20–33.
714 Li, S.Z., Zhao, S.J., Liu, X., Cao, H., Yu, S., Li, X.Y., Somerville, I., Yu, S.Y., 2018.
715 Closure of the Proto-Tethys Ocean and Early Paleozoic amalgamation of
716 microcontinental blocks in East Asia. Earth-Science Reviews 186, 37–75.
717 Liu, B., Ma, C.Q., Jiang, H.A., Guo, P., Zhang, J.Y., Xiong, F.H., 2013. Early
718 Paleozoic tectonic transition from ocean subduction to collisional orogeny in the
719 Eastern Kunlun region: Evidence from Huxiaoqin mafic rocks. Acta Petrologica
720 Sinica 29, 2093–2106 (in Chinese with English abstract).
721 Li, Z.X., Bogdanova, S.V., Collins, A.S., Davidson, A., DeWaele, B., Ernst, R.E.,
722 Fitzsimons, I.C.W., Fuck, R.A., Gladkochub, D.P., Jacobs, J., Karlstrom, K.E.,

723 Lu, S., Natapov, L.M., Pease, V., Pisarevsky, S.A., Thrane, K., Vernikovsky, V.,
724 2008a. Assembly, configuration, and break-up history of Rodinia: a synthesis.
725 Precambrian Research 160, 179–210.
726 Li, X.H., Li, W.X., Li, Z.X., Liu, Y., 2008b. 850-790 Ma bimodal volcanic and
727 intrusive rocks in northern Zhejiang, South China: a major episode of continental
728 rift magmatism during the breakup of Rodinia. Lithos 102, 341–357.
729 Lu, L., Wu, Z.H., Hu, D.G., Barosh. P.J., Hao, S., Zhou, C.J., 2010. Zircon U-Pb age
730 for rhyolite of the Maoniushan Formation and its tectonic significance in the East
731 Kunlun Mountains. Acta Petrologica Sinica 26 (4), 1150–1158 (in Chinese with
732 English abstract).
733 Ludwig, K.R., 2003. User's manual for Isoplot 3.00: a geochronological toolkit for
734 Microsoft Excel (No. 4). Kenneth R. Ludwig.
735 Metcalfe, I., 2013. Gondwana dispersion and Asian accretion: Tectonic and
736 palaeogeographic evolution of eastern Tethys. Journal of Asian Earth Sciences 66,
737 1–33.
738 Morency, C., Doin, M.-P., Dumoulin, C., 2002. Convective destabilization of a
739 thickened continental lithosphere. Earth and Planetary Science Letters 202,
740 303–320.
741 Meng, F.C., Zhang, J.X., Cui, M.H., 2013. Discovery of Early Paleozoic eclogite from
742 the East Kunlun, Western China and its tectonic significance. Gondwana
743 Research 23, 825–836.
744 Muravyeva, N.S., Belyatsky, B.V., Senin, V.G., Ivanov, A.V., 2014. Sr-Nd-Pb isotope

systematics and clinopyroxene-host disequilibrium in ultra-potassic magmas from Toro-Ankole and Virunga, East-African Rift: Implications for magma mixing and source heterogeneity. Lithos 210–211, 260–277.

Macera, P.M., Gasperini, D., Ranalli, G., Mahatsent, R., 2008. Slab detachment and mantle plume upwelling in subduction zones: an example from the Italian South-Eastern Alps. Journal of Geodynamics 45, 32–48.

Melluso, L., Mahoney, J.J., Dallai, L., 2006. Mantle sources and crustal input as recorded in high-Mg Deccan Traps basalts of Gujarat (India). Lithos 89, 259–274.

Mühe, R., Bohrmann, H., Garbe-Schönberg, D., Kassens, H., 1997. E-MORB glasses from the Gakkel Ridge (Arctic Ocean) at 87°N: evidence for the Earth's most northerly volcanic activity. Earth and Planetary Sciences Letters 152 (1), 1–9.

Morimoto, N., 1988. Nomenclature of pyroxenes. Mineralogy and Petrology 39, 55–76.

Miyashiro, A., 1974. Volcanic rock series in island arcs and active continental margins. American Journal of Science 274 (4), 321–355.

Nimis, P., Taylor, W.R., 2000. Single clinopyroxene thermobarometry for garnet peridotites: Part I. Calibration and testing of a Cr-in-Cpx barometer and an enstatite-in-cpx thermometer. Contributions to Mineralogy and Petrology 139, 541–554.

Pei, X.Z., Li, R.B., Li, Z.C., Liu, C.J., Chen, Y.X., Pei, L., Liu, Z.Q., Chen, G.C., Li, X.B., Wang, M., 2018. Composition feature and formation process of

767 Buqingshan composite accretionary mélange belt in southern margin of East
768 Kunlun orogen. Earth Science 43 (12): 4498–4520 (in Chinese with English
769 abstract).
770 Pearce, J.A., 2008. Geochemical fingerprinting of oceanic basalts with application to
771 ophiolite classification and the search for Archean oceanic crust. Lithos 100,
772 14–48.
773 Pearce, J.A., Stern, R.J., Bloomer, S.H., Fryer, P., 2005. Geochemical mapping of the
774 Mariana arc-basin system: implications for the nature and distribution of
775 subduction components. Geochemistry Geophysics Geosystems 6, Q07006.
776 http://dx.doi.org/10.1029/ 2004GC000895.
777 Prelević, D., Akal, C., Foley, S.F., Romer, R.L., Stracke, A., Van Den Bogaard, P.,
778 2012. Ultrapotassic Mafic Rocks as Geochemical Proxies for Post-collisional
779 Dynamics of Orogenic Lithospheric Mantle: the Case of Southwestern Anatolia,
780 Turkey. Journal of Petrology 53, 1019–1055.
781 Qi, S.S., Song, S.G., Shi, L.C., Cai, H.J., Hu, S.C., 2014. Discovery and its geological
782 significance of early Paleozoic eclogite in Xiarihamu-Suhaitu area, western part
783 of the east Kunlun. Acta Petrologica Sinica 30, 3345–3356 (in Chinese with
784 English abstract).
785 Rudnick, R.L., Gao, S., 2003. The composition of the continental crust. In: Rudnick,
786 R.L. (Ed.), The Crust. Elsevier-Pergamon, Oxford, pp. 1–64.
787 Rublee, V.J., 1994. Chemical Petrology, Mineralogy and Structure of the Tulameen
788 Complex, Princeton Area, British Colombia. Unpublished M.Sc. Thesis.

University of Ottawa, Canada, p. 179.

Song, Y.T., Su, L., Dong, J.L., Song, S.G., Allen, M.B., Wang, C., Hu, X.L., 2020. Detrital zircons from Late Paleozoic to Triassic sedimentary rocks of the Gongshan-Baoshan Block, SE Tibet: Implications for episodic crustal growth of Eastern Gondwana. Journal of Asian Earth Sciences 188, 104106.

Song, S.G., Bi, H.Z., Qi, S.S., Yang, L.M., Allen, M.B., Niu, Y.L., Su, L., Li, W.F., 2018. HP-UHP metamorphic belt in the East Kunlun orogen: final closure of the Proto-Tethys Ocean and formation of Pan-North-China Continent. Journal of Petrology 59 (11), 2043–2060.

Song, S.G., Yang, L.M., Zhang, Y.Q., Niu, Y.L., Wang, C., Su, L., Gao, Y. L., 2017. Qi-Qin Accretionary Belt in Central China Orogen: accretion by trench jam of oceanic plateau and formation of intra-oceanic arc in the Early Paleozoic Qin-Qi-Kun Ocean. Science Bulletin 62, 1035–1038.

Song, S.G., Wang, M.M., Xu, X., Wang, C., Niu, Y.L., Allen, M.B., Su, L., 2015a. Ophiolites in the Xing'an-Inner Mongolia accretionary belt of the CAOB: Implications for two cycles of seafloor spreading and accretionary orogenic events. Tectonics 34, 2221–2245.

Song, S., Wang, M., Wang, C., Niu, Y., 2015b. Magmatism during continental collision, subduction, exhumation and mountain collapse in collisional orogenic belts and continental net growth: A perspective. Science China Earth Sciences 58, 1284–1304.

Stampfli, G.M., Borel, G.D., 2002. A plate tectonic model for the Paleozoic and

Mesozoic constrained by dynamic Plate boundaries and restored synthetic oceanic isochrons. Earth and Planetary Science Letters 196 (1–2), 17–33.

Sun, S.S., McDonough, W.F., 1989. Chemical and isotopic systematics of oceanic basalts: implications for mantle composition and processes. Geological Society of London, Special Publication 42, 313–345.

Smith, J.V., Brown, W.L., 1988. Feldspar Minerals: Second Revised and Extended Edition. Springer Verlag, Berlin Heidelberg, New York, London, Paris, Tokyo.

Shervais, J.W., 1982. Ti-V plots and the petrogenesis of modern and ophiolitic lavas. Earth and Planetary Science Letters 59, 101–118.

Tian, G.K., Meng, F.C., Fan, Y.Z., Liu, Q., Duan, X.P., 2016. The characteristics of early Paleozoic post-orogenic granite in the east Kunlun orogen: a case study of Dagangou granite. Acta Petrologica et Mineralogica 35, 371–390 (in Chinese with English abstract).

von Raumer, J.F., Stampfli, G.M., 2008. The birth of the Rheic Ocean-Early Palaeozoic subsidence patterns and subsequent tectonic plate scenarios. Tectonophysics 461 (1-4), 9–20.

von Blanckenburg, F., Davies, J.H., 1995. Slab break off: a model for syncollisional magmatism and tectonics in the Alps. Tectonics 14 (1), 120–131.

Wan, Y., Zhang, J., Yang, J., Xu, Z., 2006. Geochemistry of high-grade metamorphic rocks of the North Qaidam mountains and their geological significance. Journal of Asian Earth Sciences 28, 174–184.

Wilson, M., 1989. Igneous Petrogenesis. Unwin Hyman, London.

833 Winchester, J.A., Floyd, P.A., 1976. Geochemical magma type discrimination:
834 application to altered and metamorphosed basic igneous rocks. Earth and
835 Planetary Science Letters 28, 459–469.
836 Xia, W.C., Zhang, N., Yuan, X.P., Fan, L.S., Zhang, B.S., 2001. Cenozoic Qaidam
837 basin, China: a stronger tectonic inversed, extensional rifted basin. AAPG Bull.
838 85, 715–736.
839 Xiong, F., Ma, C., Jiang, H.a., Liu, B., Huang, J., 2014. Geochronology and
840 geochemistry of Middle Devonian mafic dykes in the East Kunlun orogenic belt,
841 Northern Tibet Plateau: Implications for the transition from Prototethys to
842 Paleotethys orogeny. Chemie der Erde-Geochemistry 74, 225–235.
843 Xin, W., Sun, F.Y., Li, L., Yan, J.M., Zhang, Y.T., Wang, Y.C., Shen, TS., Yang, Y.J.,
844 2018. The Wulonggou metaluminous A_2-type granites in the Eastern Kunlun
845 Orogenic Belt, NW China: Rejuvenation of subduction-related felsic crust and
846 implications for post-collision extension. Lithos 312–313, 108–127.
847 Yang, L., Zhou, H.W., Zhu, Y.H., Dai, X., Lin, Q.X., Ma, Z.Q., Jian, K.K., Zhang,
848 M.Y., 2014. Geochemical characteristics and LA-ICP-MS zircon U-Pb ages of
849 intermediate to mafic dyke swarms in Haxiya area, Golmud, Qinghai Province.
850 Geological Bulletin of China 33, 804–819 (in Chinese with English abstract).
851 Yang, J.S., Robinson, P.T., Jiang, C.F., Xu, Z.Q., 1996. Ophiolites of the Kunlun
852 mountains, China and their tectonic implications. Tectonophysics 258, 215–231.
853 Yuan, C., Zhou, M.F., Sun, M., Zhao, Y.J., Wilde, S., Long, X.P., Yan, D.P., 2010.
854 Triassic granitoids in the eastern Songpan Ganzi Fold Belt, SW China: magmatic

response to geodynamics of the deep lithosphere. Earth and Planetary Science Letters 290, 481–492.

Zhao, G.C., Wang, Y.J., Huang, B.C., Dong, Y.P., Li, S.Z., Zhang, G.W., Yu, S., 2018a. Geological reconstructions of the East Asian blocks: From the breakup of Rodinia to the assembly of Pangea. Earth-Science Reviews 186, 262–286.

Zhao, Z., Wei, J., Santosh, M., Liang, S., Fu, L., Zhao, S., Li, H., 2018b. Late Devonian postcollisional magmatism in the ultrahigh- pressure metamorphic belt, Xitieshan terrane, NW China. Geological Society of America Bulletin 130, 999–1016.

Zhao, Z., Wei, J., Fu, L., Liang, S., Zhao, S., 2017. The Early Paleozoic Xitieshan syn-collisional granite in the North Qaidam ultrahigh-pressure metamorphic belt, NW China: Petrogenesis and implications for continental crust growth. Lithos 278–281, 140–152.

Zhang, G.L., Luo, Q., Zhao, J., Jackson, M.G., Guo, L.S., Zhong, L.F., 2018. Geochemical nature of sub-ridge mantle and opening dynamics of the South China Sea. Earth and Planetary Science Letters 489, 145–155.

Zhang, J., Ma, C., Xiong, F., Liu, B., Li, J., Pan, Y., 2014. Early Paleozoic high-Mg diorite-granodiorite in the eastern Kunlun Orogen, western China: Response to continental collision and slab break-off. Lithos 210–211, 129–146.

Zhai, Q.G., Jahn, B.M., Wang, J., Su, L., Mo, X.-X., Wang, K.-L., Tang, S.-H., Lee, H.-Y., 2013. The Carboniferous ophiolite in the middle of the Qiangtang terrane, Northern Tibet: SHRIMP U-Pb dating, geochemical and Sr-Nd-Hf isotopic

characteristics. Lithos 168-169, 186–199.

Zhai, Q.G., Zhang, R.Y., Jahn, B.M., Li, C., Song, S.G., Wang, J., 2011. Triassic eclogites from central Qiangtang, northern Tibet, China: petrology, geochronology and metamorphic P-T path. Lithos 125 (1–2), 173–189.

Zhao, J.-H., Zhou, M.-F., 2007. Geochemistry of Neoproterozoic mafic intrusions in the Panzhihua district (Sichuan Province, SW China): implications for subduction-related metasomatism in the upper mantle. Precambrian Research 152, 27–47.

Zheng, Z., Chen, Y.J., Deng, X.H., Yue, S.W., Chen, H.J., Wang, Q.F., 2018. Origin of the Bashierxi monzogranite, Qimantagh, East Kunlun Orogen, NW China: a magmatic response to the evolution of the Proto-Tethys Ocean. Lithos 296-299, 181–194.

Zhong, S., Feng, C., Seltmann, R., Li, D., 2017. Middle Devonian volcanic rocks in the Weibao Cu-Pb-Zn deposit, East Kunlun Mountains, NW China: Zircon chronology and tectonic implications. Ore Geology Reviews 84, 309–327.

Zhu, D.C., Wang, Q., Zhao, Z.D., Chung, S.L., Cawood, P.A., Niu, Y.L., Liu, S.A., Wu, F.Y., Mo, X.X., 2015. Magmatic record of India–Asia collision. Scientific Reports 5, 14289.

Zhu, W.-G., Zhong, H., Li, X.-H., Deng, H.-L., He, D.-F., Wu, K.-W., Bai, Z.-J., 2008. SHRIMP zircon U-Pb geochronology, elemental, and Nd isotopic geochemistry of the Neoproterozoic mafic dykes in the Yanbian area, SW China. Precambrian Research 164, 66–85.

Zhou, B., Dong, Y., Zhang, F., Yang, Z., Sun, S., He, D., 2016. Geochemistry and zircon U-Pb geochronology of granitoids in the East Kunlun Orogenic Belt, northern Tibetan Plateau: origin and tectonic implications. Journal of Asian Earth Sciences 130, 265–281.

Zhou, J.B., Li, X.-H., Ge, W.C., Li, Z.-X., 2007. Age and origin of middle Neoproterozoic mafic magmatism in southern Yangtze Block and relevance to the break-up of Rodinia. Gondwana Research 12, 184–197.

Figure Captions

Fig. 1. (A) Sketch map showing major tectonic units of mainland China, showing the location of East Kunlun in northwest China, modified after Song et al. (2017). (B) Simplified geological map of the East Kunlun Orogen and Qaidam-Qilian Orogenic Belt modified after Song et al. (2018). CAOB = Central Asian Orogenic Belt, CCOB = Central China Orogenic Belt, NCC = North China Craton, SCC = South China Craton, TB = Tarim Block, QT = Qiangtang Block, SU = Sibumasu block, NQAB = North Qilian Accretionary Belt, SQAB = South Qilian Accretionary Belt, NQUB = North Qaidam UHPM Belt.

915

916 **Fig. 2.** (A) Geological map of the Tatuo area, modified after BGQP (1973). (B) Stratigraphic

917 columns from the Kehete-Tatuo area, mainly showing the Silurian-Devonian volcanic-sedimentary

918 strata. Pre. = Precambrian, Me. = Mesozoic.

Fig. 3. Field and photomicrographs of the Tatuo mafic igneous rocks. (A) and (B) Field occurrence of basaltic lavas. (C) and (D) Basalts showing phenocrysts in a matrix, composed of oriented fine- to micro-grained plagioclase, clinopyroxene, opaque mineral and altered minerals (cross-polarized light). (E) Dolerites showing a fine-grained ophitic texture (cross-polarized light). (F) and (G) Field occurrence of diabase dykes. (H) and (I) Diabase dykes showing fine- to medium-grained ophitic textures (cross-polarized light).

926

927 **Fig. 4.** (A) An-Ab-Or triangular diagram (Smith and Brown, 1988) showing the compositions of

928 plagioclase for the Tatuo diabase dykes. (B) Wo-En-Fs diagram (Morimoto, 1988) for

929 clinopyroxene for the Tatuo diabase dykes. (C) Alz (percentage of tetrahedral sites occupied by Al)

930 versus TiO_2 (wt.%) diagram for the Tatuo diabase dykes. Tulameen data are from Rublee (1994).

931 Rift-related Cpx compositions are from Zhu et al. (2008), Li et al. (2008b) and Muravyeva et al.

932 (2014).

Fig. 5. (A) Zr/TiO_2 versus Nb/Y (Winchester and Floyd, 1976), (B) TiO_2 versus FeO_T/MgO (Miyashiro, 1974) and (C) Sm/Yb versus Ti/Y diagrams for the Tatuo mafic igneous rocks.

936

937 **Fig. 6.** Chondrite-normalized REE and primitive mantle-nomalized multi-element patterns for the

938 Tatuo mafic igneous rocks. Chondrite and primitive mantle normalizing values and N-MORB,

939 E-MORB and OIB data are after Sun and McDonough (1989). Literature data are from George et

940 al. (2003), Pearce et al. (2005) and Melluso et al. (2006).

941

942 **Fig. 7.** CL images of representative zircon grains and concordia diagrams for the Tatuo mafic

943 igneous rocks.

944

945 **Fig. 8.** (A) $\varepsilon_{Nd}(t)$ versus $I_{Sr}(t)$, and (B) $\varepsilon_{Nd}(t)$ versus Mg# diagrams for the Tatuo mafic igneous

946 rocks.

947

948 **Fig. 9.** Plots of MgO versus SiO_2 (A), FeO_T versus SiO_2 (B), Al_2O_3 versus SiO_2 (C), TiO_2 versus

949 MgO (D), Ni versus Cr (E) and V versus Cr (F) for the Tatuo mafic igneous rocks.

Fig. 10. (A) Th/Yb versus Nb/Yb (Pearce, 2008), (B) Nb/Th versus Na/La, (C) Nb/Zr versus Th/Zr (Zhao and Zhou, 2007) and (D) Th/Nb versus $\varepsilon_{Nd}(t)$ diagrams for the Tatuo mafic igneous rocks. Primitive mantle (PM), N-MORB, E-MORB and OIB data are after Sun and McDonough (1989). The data for the lower and upper continental crust are from Rudnick and Gao (2003). The continental crust composition (Th=22.9 ppm, Nb=18.5 ppm and $\varepsilon_{Nd}(t)$=-8.06) is represented by the Wanbaogou sandstone (unpublished data). The SCLM composition (Th=0.08 ppm, Nb=0.12 ppm and $\varepsilon_{Nd}(t)$=-1.39) is from the Xiarihamu mafic-ultramafic intrusion in the EKO and is after Jiang et al. (2015). The asthenospheric mantle composition (Th=0.44 ppm, Nb=6.35 ppm and $\varepsilon_{Nd}(t)$=+7.0) is from the Gakkel Ridge proposed by Mühe et al. (1997). LCC = Lower continental crust. UCC = Upper continental crust. SCLM = Subcontinental lithospheric mantle.

961

962 **Fig. 11.** (A) Tb/Yb versus La/Yb (George and Rogers, 2002) and (B) V versus Ti/1000 (Shervais,

963 1982) diagrams for the Tatuo mafic igneous rocks. (C) The relative probability density and (D)

964 zircon $\varepsilon_{Hf}(t)$ versus Age (Ma) diagrams for the Cambrian to Devonian magmatic rocks in the EKO.

965 Age and zircon $\varepsilon_{Hf}(t)$ data are from Tian et al. (2016), Zhou et al. (2016), Zheng et al. (2018), Xin

966 et al. (2018) and references therein and Chen et al. (2020).

967

968 **Fig. 12.** Schematic cartoons showing the tectonic evolution of the EKO from the Cambrian to

969 Devonian. QB = Qaidam Block, EKB = East Kunlun Block, NQTB = North Qiangtang Block.

Fig.1-R3

Click here to download high resolution image

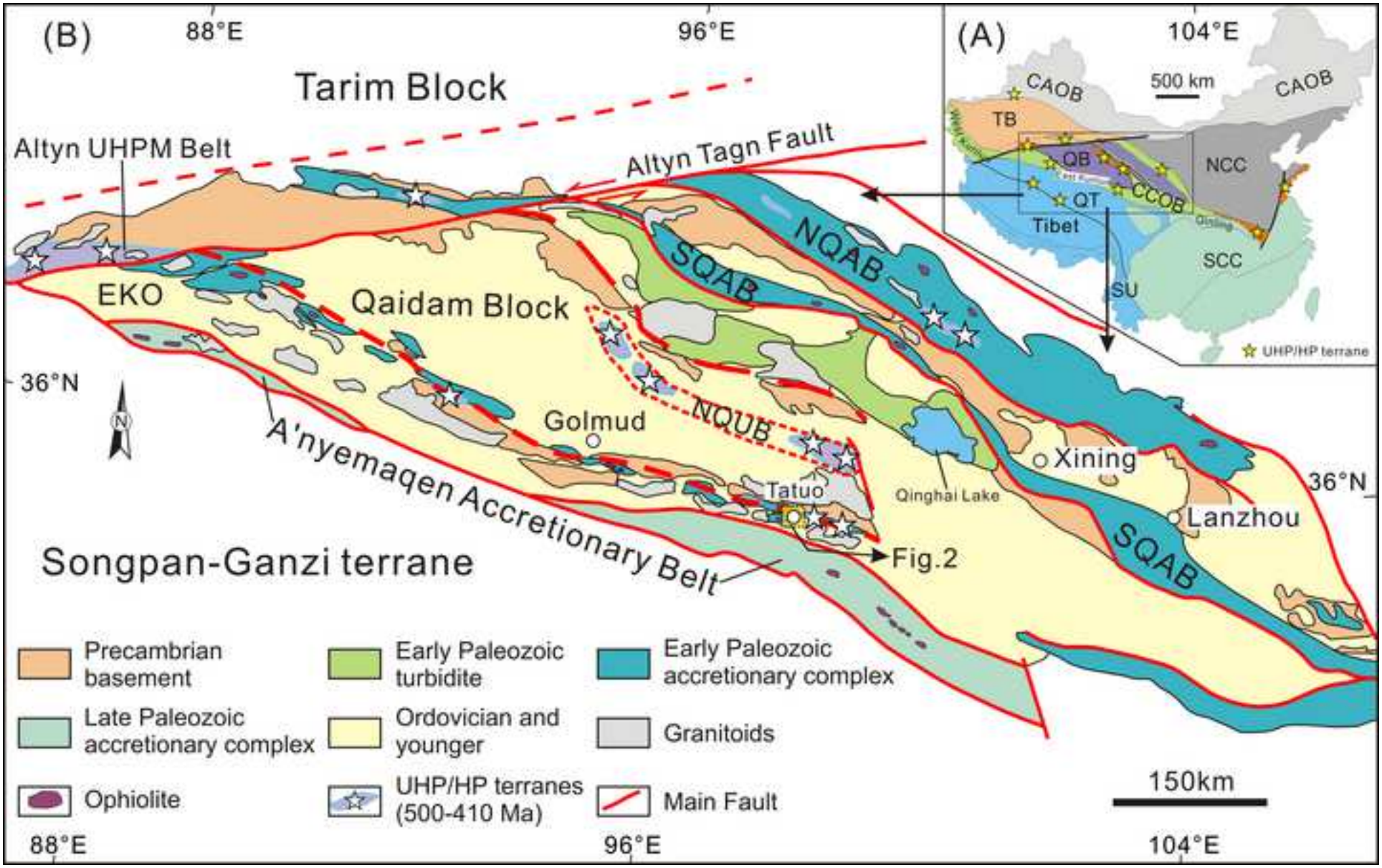

Fig.2-R3

Click here to download high resolution image

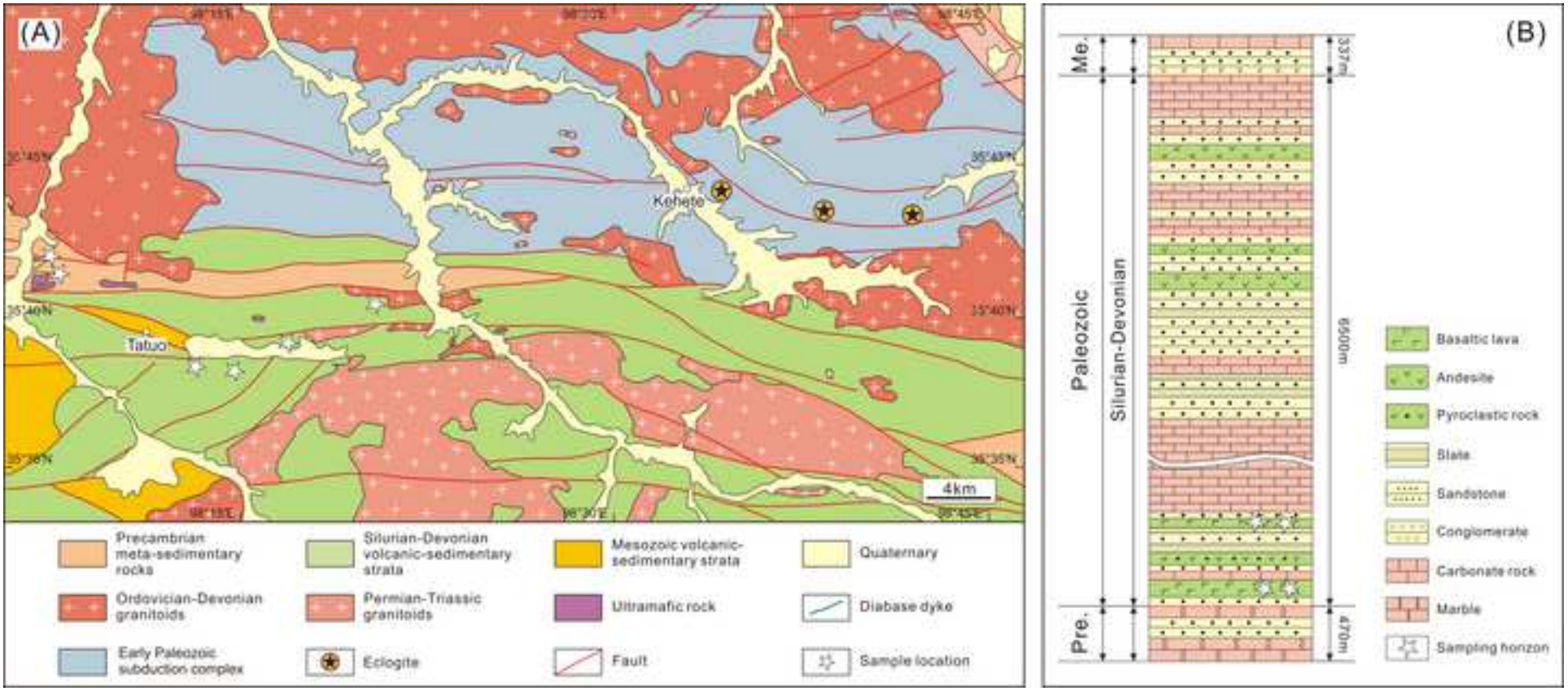

Fig.3-R3

Click here to download high resolution image

Fig.4-R3

Click here to download high resolution image

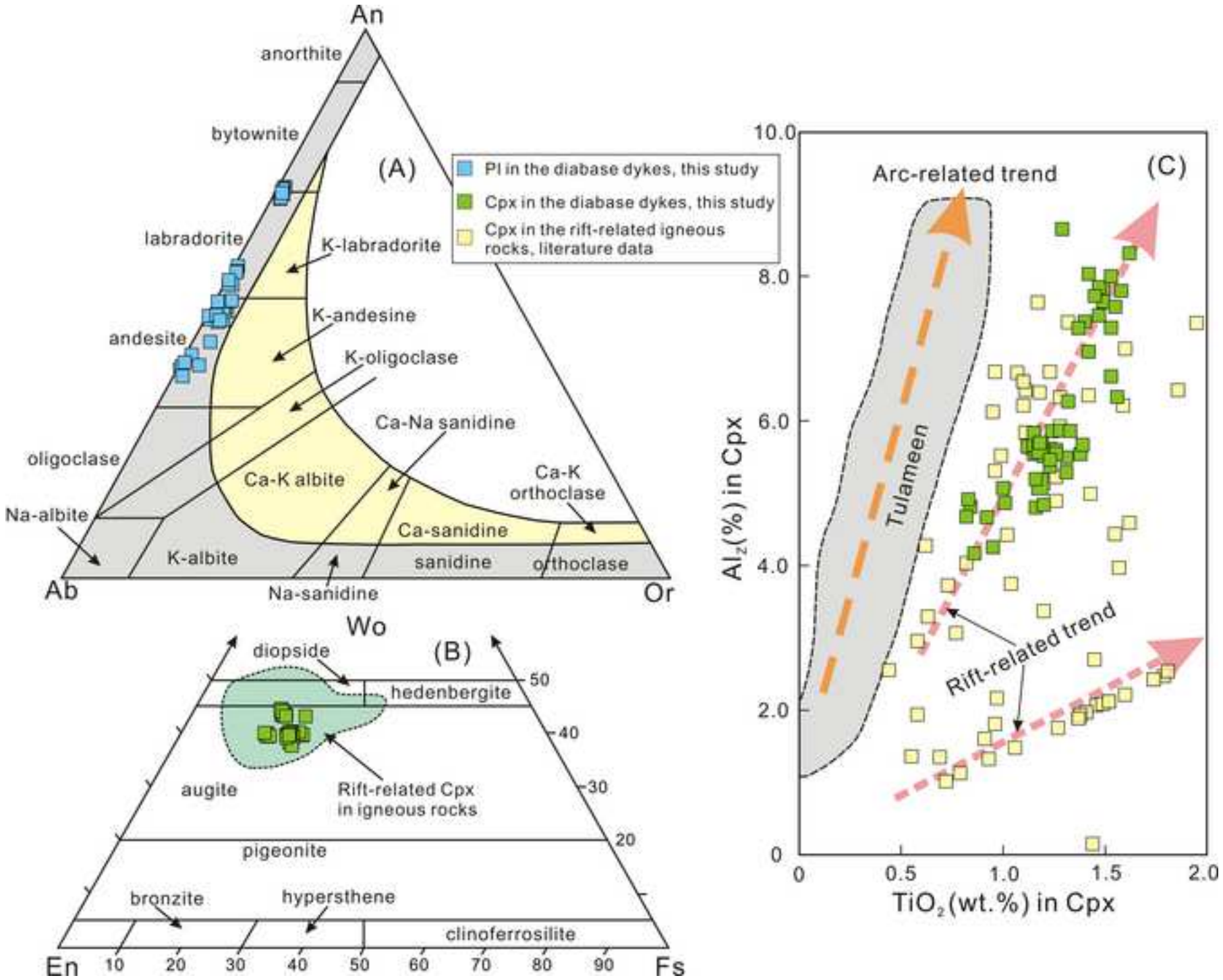

Fig.5-R3

Click here to download high resolution image

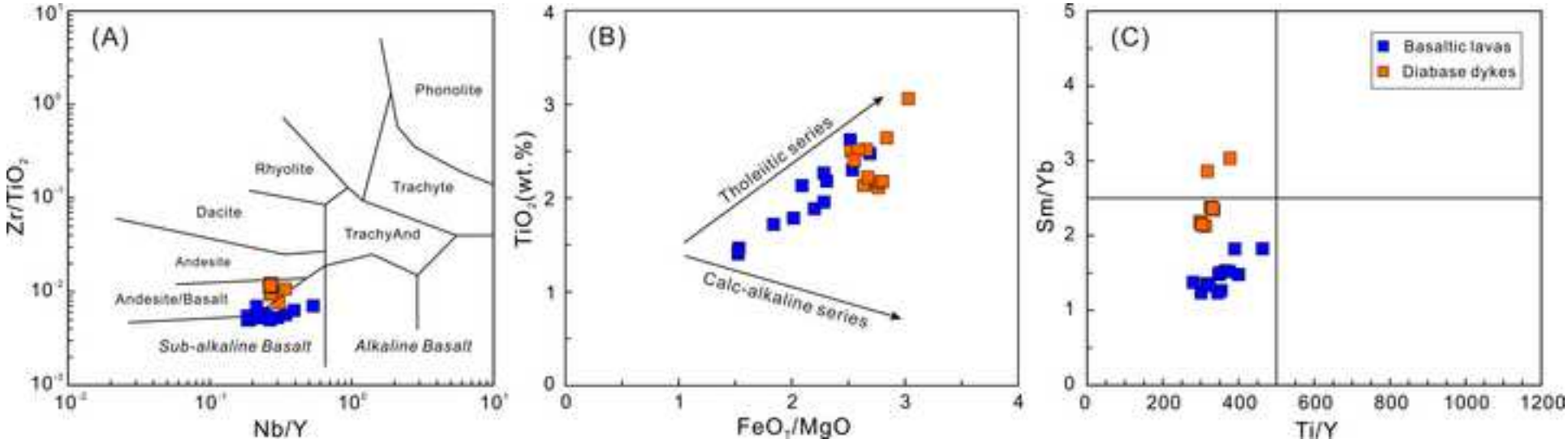

Fig.6-R3

Click here to download high resolution image

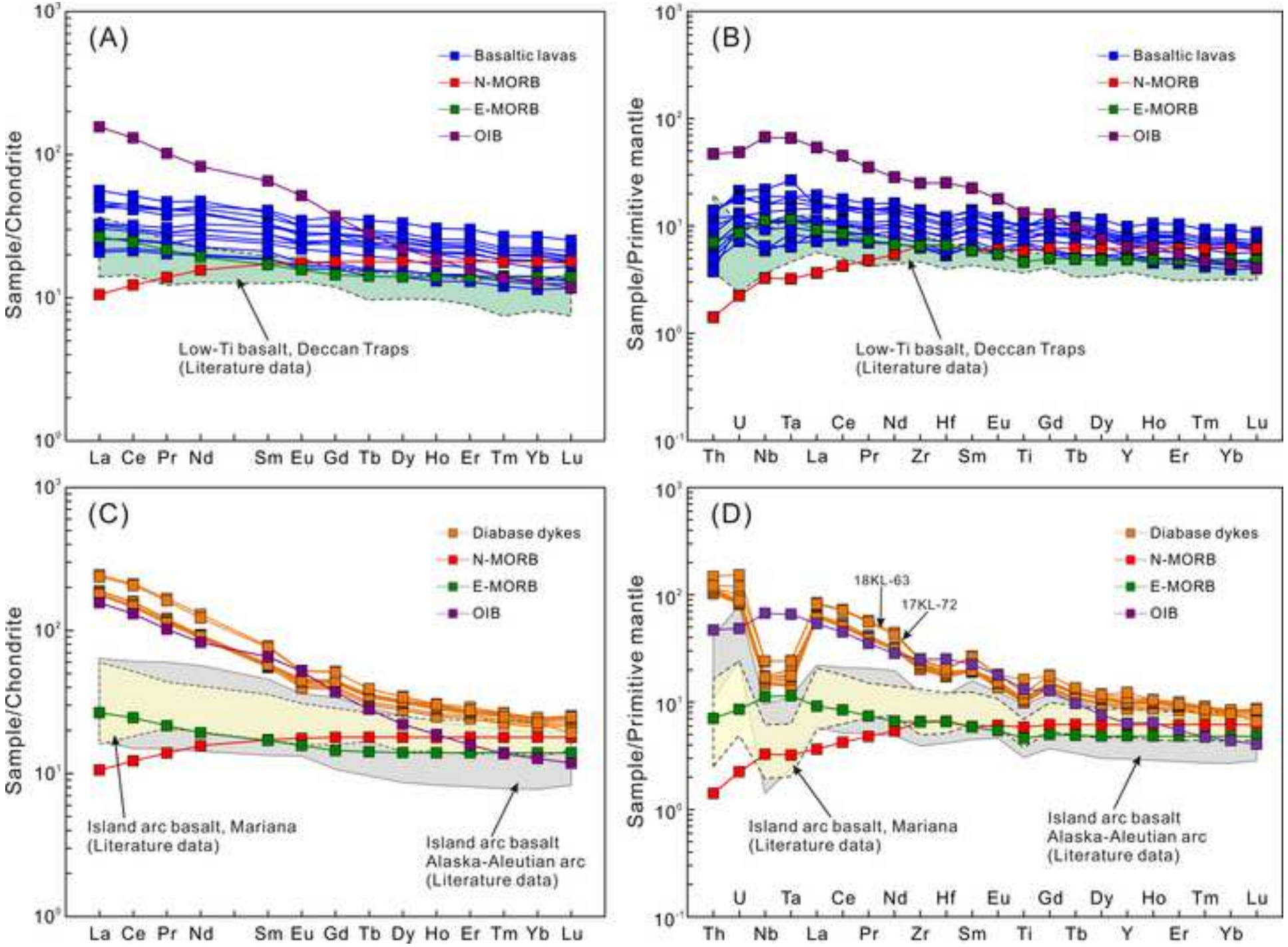

Fig.7-R3

Click here to download high resolution image

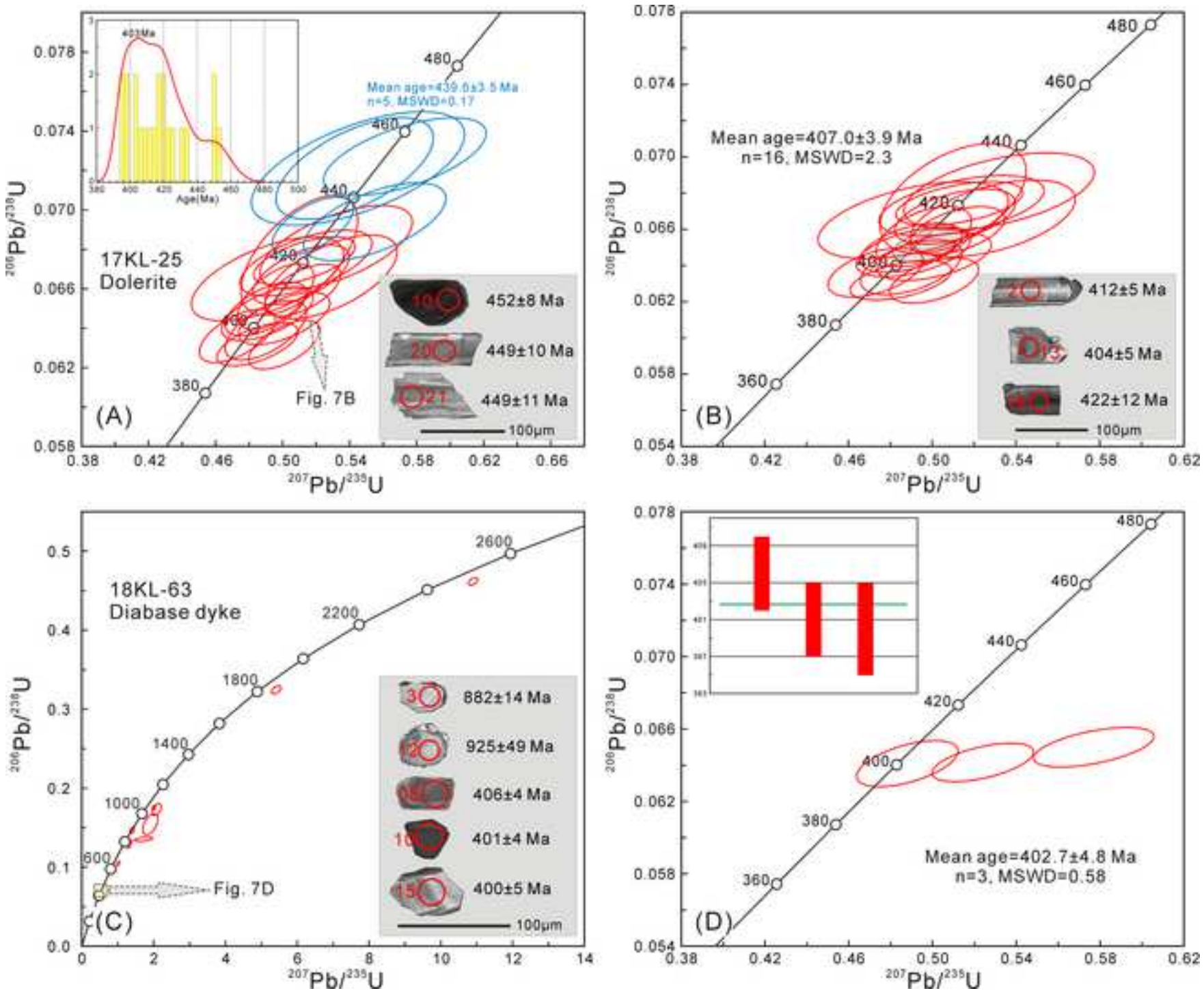

Fig.8-R3

Click here to download high resolution image

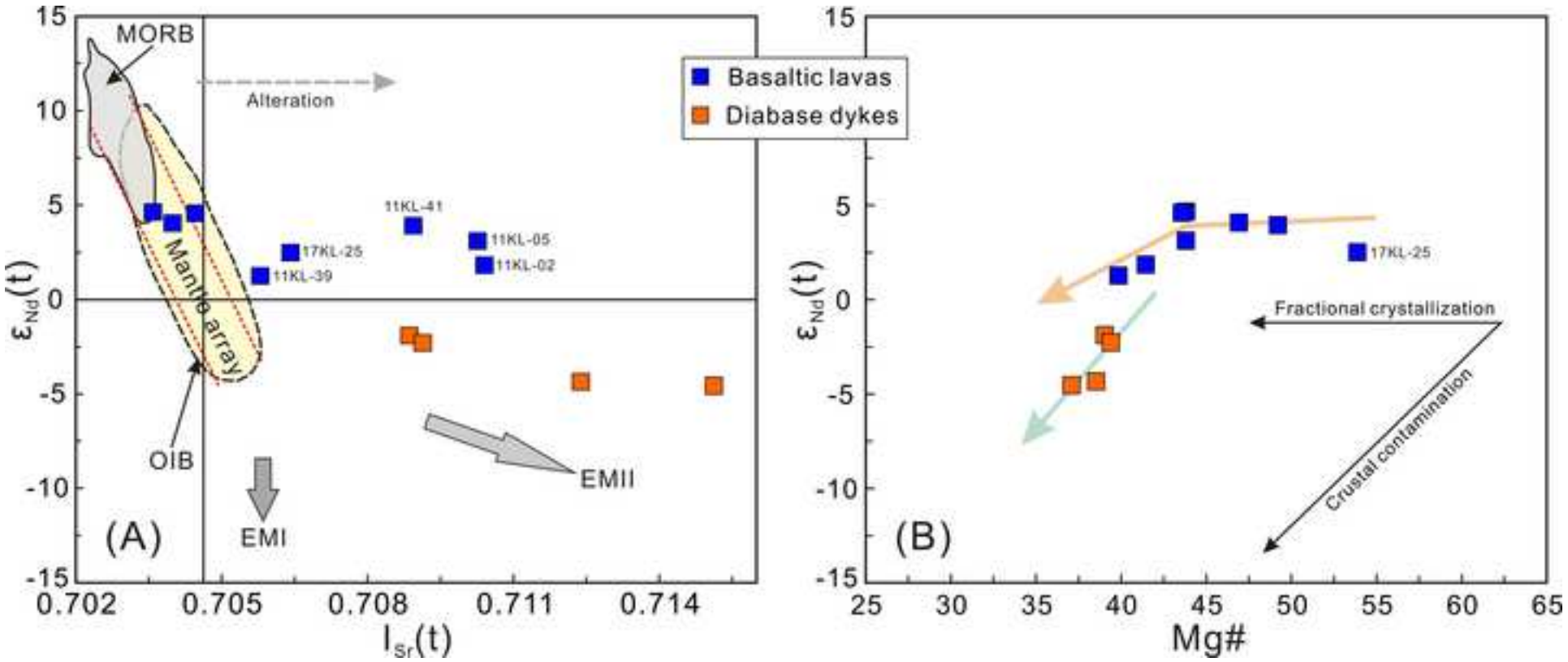

Fig.9-R3

Click here to download high resolution image

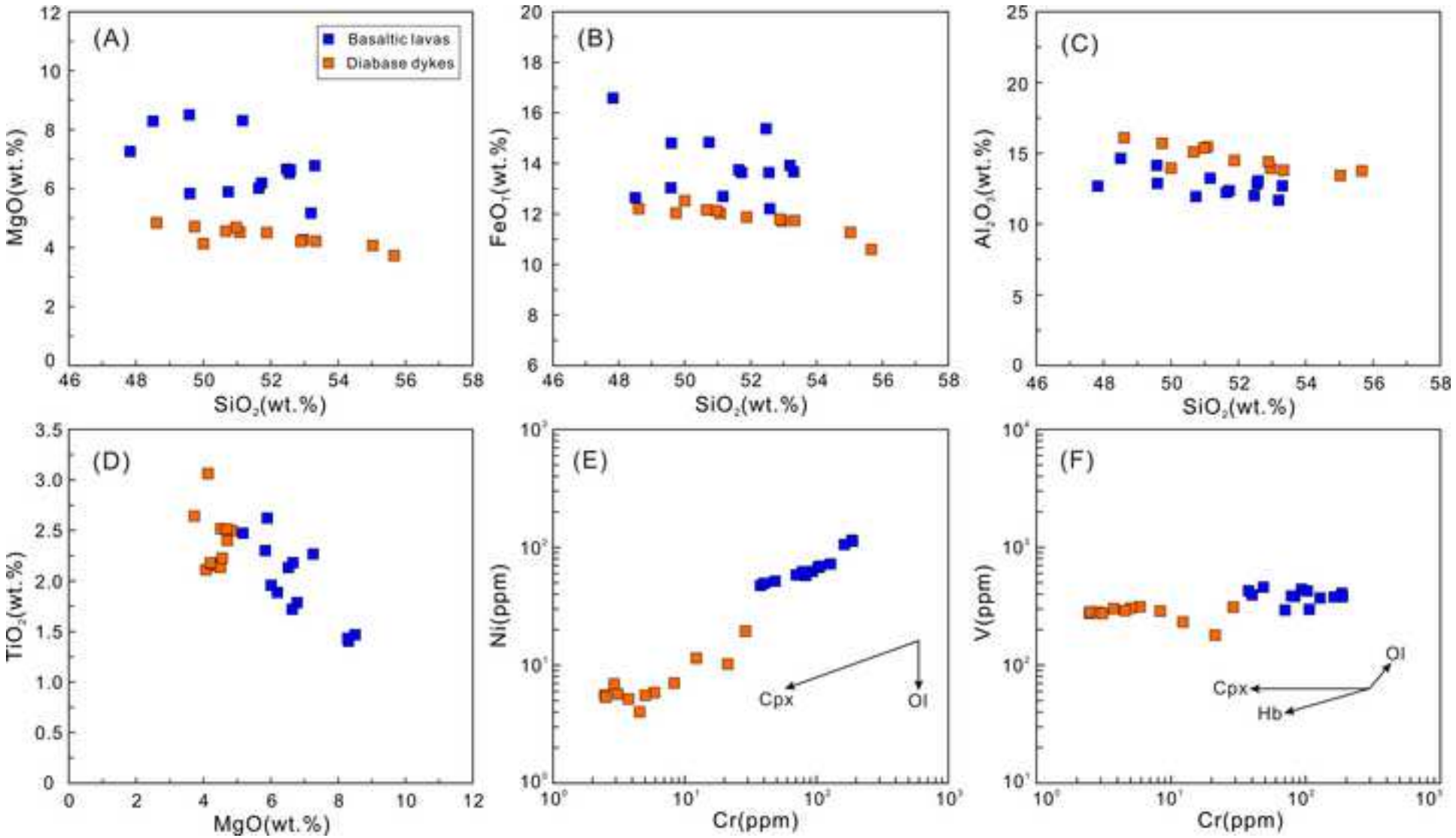

Fig.10-R3

Click here to download high resolution image

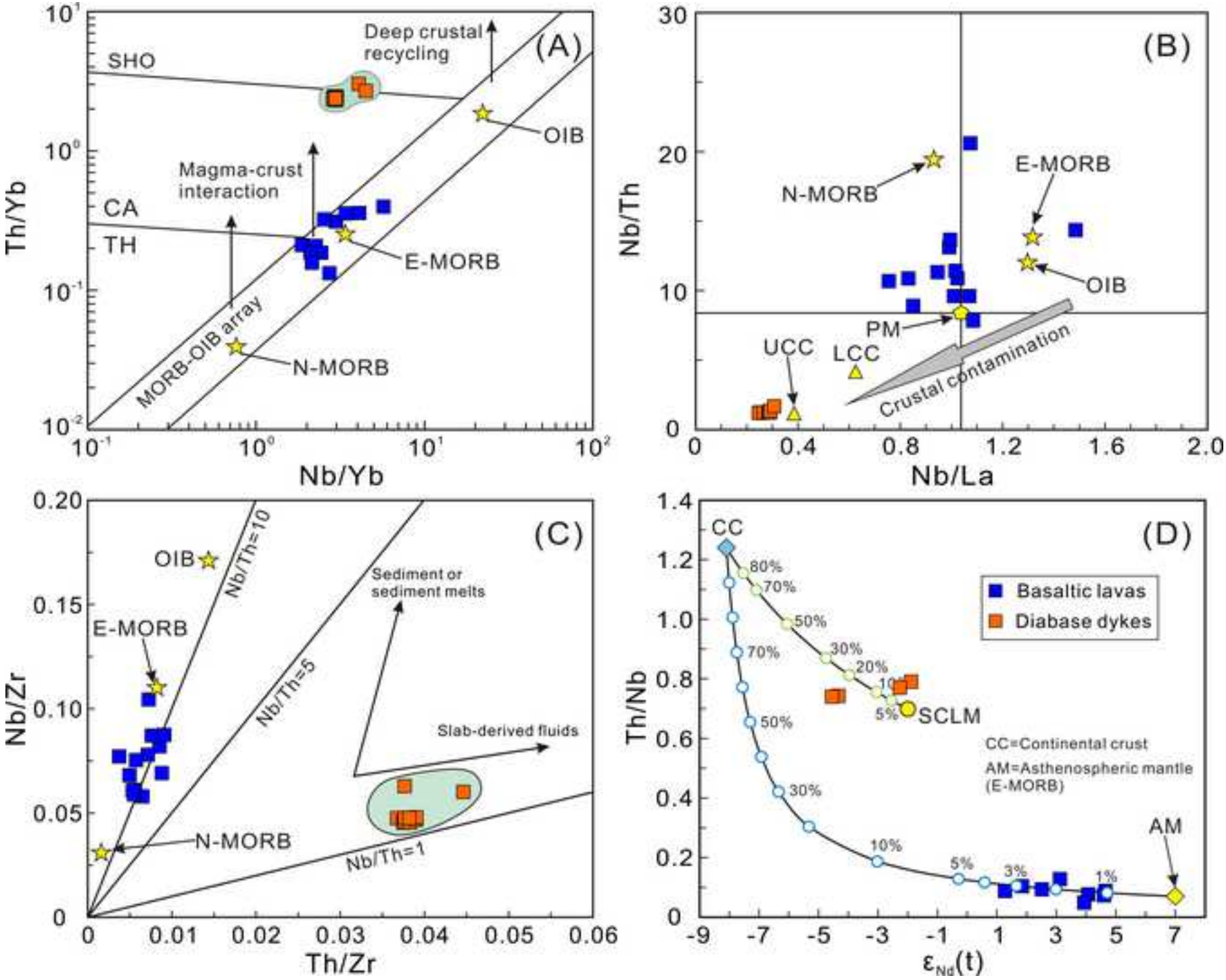

Fig.11-R3

Click here to download high resolution image

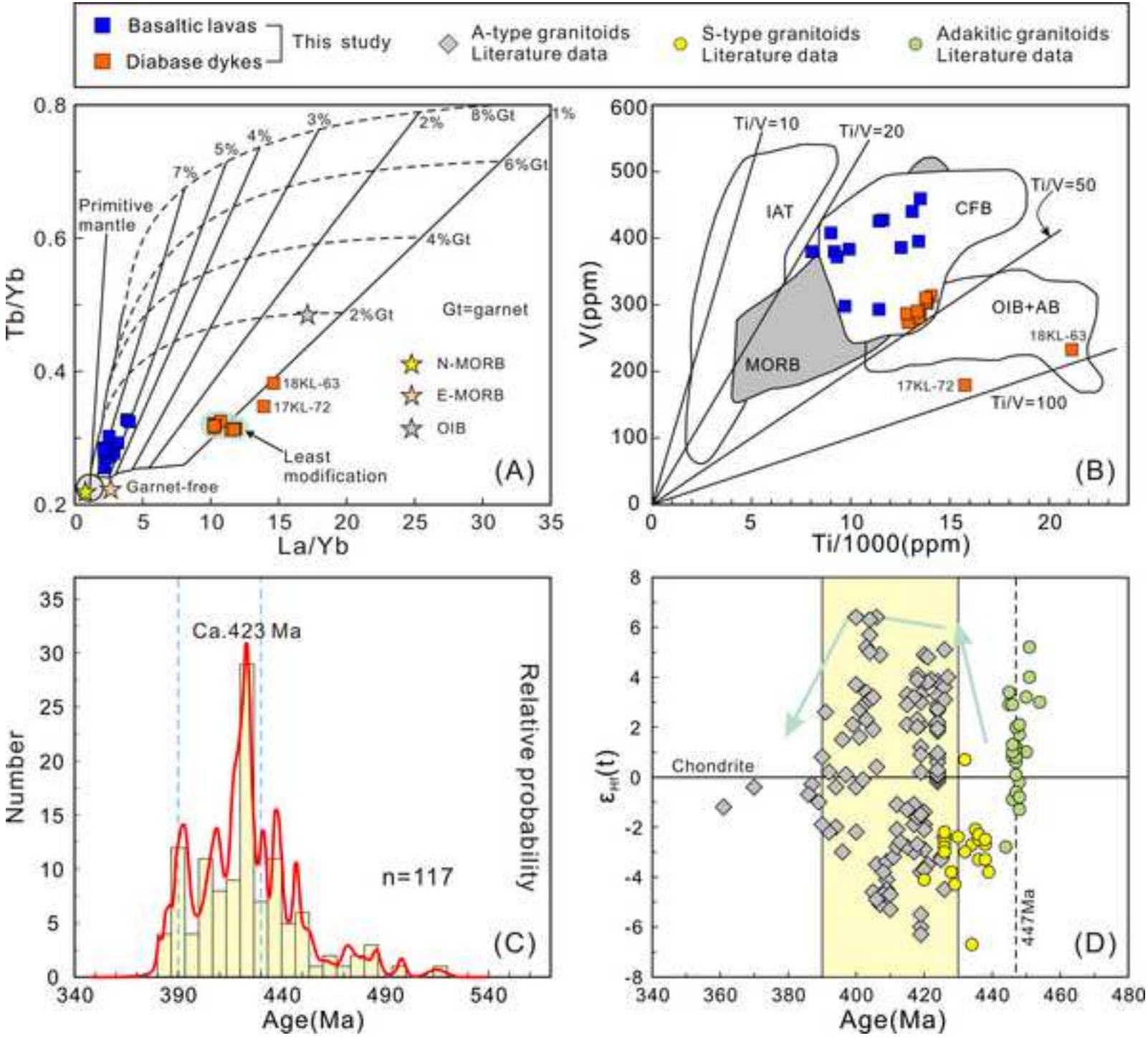

Fig.12-R3

Click here to download high resolution image

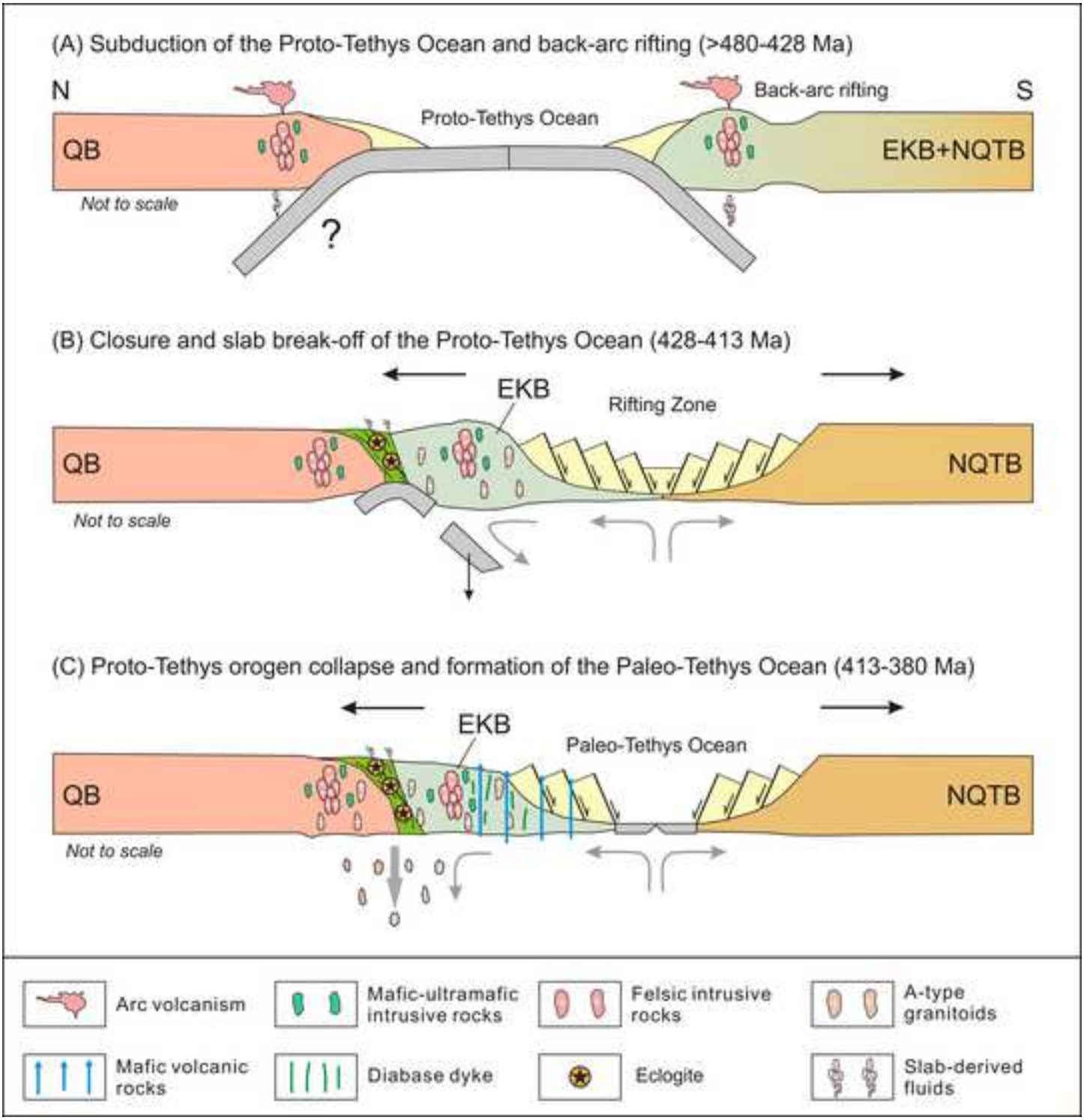

Table S1-R3

Click here to download Supplementary material/Appendix (Files for online publication only): Table S1-R3.xlsx

Table S2-R3

Click here to download Supplementary material/Appendix (Files for online publication only): Table S2-R3.xlsx

Table S3-R3

Click here to download Supplementary material/Appendix (Files for online publication only): Table S3-R3.xlsx

Table S4-R3

Click here to download Supplementary material/Appendix (Files for online publication only): Table S4-R3.xlsx

Table S5-R3

Click here to download Supplementary material/Appendix (Files for online publication only): Table S5-R3.xlsx

Declaration of Competing Interests

The authors declare that they have no conflicts of personal relationships or financial interests that could have appeared to influence the work reported in this paper.